

A novel order-reduced thermal-coupling electrochemical model for lithium-ion batteries

Yizhan Xie, Shuhui Wang, Zhenpo Wang, and Ximing Cheng

Citation: Chin. Phys. B, 2024, 33 (**5**): 058203. DOI: 10.1088/1674-1056/ad1f52
Journal homepage: http://cpb.iphy.ac.cn; http://iopscience.iop.org/cpb

What follows is a list of articles you may be interested in

Influence of carbon sources on the performance of carbon-coated nano-silicon

Lin Wang(王琳), Na Li(李娜), Hao-Sen Chen(陈浩森), and Wei-Li Song(宋维力)
Chin. Phys. B, 2023, 32 (**10**): 108201. DOI: 10.1088/1674-1056/acb9e9

A novel calculation strategy for optimized prediction of the reduction of electrochemical window at anode

Guochen Sun(孙国宸), Jian Gao(高健), and Hong Li(李泓)
Chin. Phys. B, 2023, 32 (**7**): 078201. DOI: 10.1088/1674-1056/accd51

Stress effect on lattice thermal conductivity of anode material $NiNb_2O_6$ for lithium-ion batteries

Ao Chen(陈奥), Hua Tong(童话), Cheng-Wei Wu(吴成伟), Guofeng Xie(谢国锋), Zhong-Xiang Xie(谢忠祥), Chang-Qing Xiang(向长青), and Wu-Xing Zhou(周五星)
Chin. Phys. B, 2023, 32 (**5**): 058201. DOI: 10.1088/1674-1056/acaa2d

Understanding the battery safety improvement enabled by a quasi-solid-state battery design

Luyu Gan(甘露雨), Rusong Chen(陈汝颂), Xiqian Yu(禹习谦), and Hong Li(李泓)
Chin. Phys. B, 2022, 31 (**11**): 118202. DOI: 10.1088/1674-1056/ac9221

Probing component contributions and internal polarization in silicon-graphite composite anode for lithium-ion batteries with an electrochemical-mechanical model

Yue Chen(陈约), Fuliang Guo(郭福亮), Lufeng Yang(杨陆峰), Jiaze Lu(卢嘉泽), Danna Liu(刘丹娜), Huayu Wang(王华宇), Jieyun Zheng(郑杰允), Xiqian Yu(禹习谦), and Hong Li(李泓)
Chin. Phys. B, 2022, 31 (**7**): 078201. DOI: 10.1088/1674-1056/ac6012

A novel order-reduced thermal-coupling electrochemical model for lithium-ion batteries

Yizhan Xie(谢奕展)[1,2,3,†], Shuhui Wang(王舒慧)[1,2,†], Zhenpo Wang(王震坡)[1,2], and Ximing Cheng(程夕明)[1,2,‡]

[1] *School of Mechanical Engineering, Beijing Institute of Technology, Beijing* 100081, *China*

[2] *National Engineering Research Center for Electric Vehicles, Beijing Institute of Technology, Beijing* 100081, *China*

[3] *The Hong Kong University of Science and Technology (Guangzhou), Sustainable Energy and Environment Thrust and Guangzhou Municipal, Key Laboratory of Materials Informatics, Guangzhou* 511400, *China*

(Received 11 November 2023; revised manuscript received 16 January 2024; accepted manuscript online 17 January 2024)

Although the single-particle model enhanced with electrolyte dynamics (SPMe) is simplified from the pseudo-two-dimensional (P2D) electrochemical model for lithium-ion batteries, it is difficult to solve the partial differential equations of solid–liquid phases in real-time applications. Moreover, working temperatures have a heavy impact on the battery behavior. Hence, a thermal-coupling SPMe is constructed. Herein, a lumped thermal model is established to estimate battery temperatures. The order of the SPMe model is reduced by using both transfer functions and truncation techniques and merged with Arrhenius equations for thermal effects. The polarization voltage drop is then modified through the use of test data because its original model is unreliable theoretically. Finally, the coupling-model parameters are extracted using genetic algorithms. Experimental results demonstrate that the proposed model produces average errors of about 42 mV under 15 constant current conditions and 15 mV under nine dynamic conditions, respectively. This new electrochemical-thermal coupling model is reliable and expected to be used for onboard applications.

Keywords: lithium-ion batteries, order-reduced electrochemical models, SPMe, thermal-coupling model, transient polarization voltage drop

PACS: 82.47.Wx **DOI:** 10.1088/1674-1056/ad1f52

1. Introduction

It is crucial for a lithium-ion battery model to adapt to working conditions including temperature and current variations with high real-time computational efficiency in onboard applications. Electrochemical models of lithium-ion batteries are widely recognized in industries due to their strong physical characterization. These models primarily include the pseudo-two-dimensional (P2D) model and its two simplified models, namely the single particle model (SPM) and its electrolyte dynamics enhanced model (SPMe). However, these electrochemical models face challenges, such as the large number of parameters, tight coupling of variables, and difficulty in solving partial differential equations, which limit their applicability in battery management systems (BMS). The battery electrochemical models can be reduced to three orders or less.[1–8] The general order reduction methods include polynomial approximation,[2,3,9,10] Padé approximation[4,11–13] and residue grouping methods.[14,15] The main idea of polynomial approximation is that the ion concentration obeys a polynomial distribution inside the control volume. Therefore, both volume averages and control points can be utilized to make a mapping between polynomial coefficients and external inputs.[1] This is a steady-state approximate spatial solution method that satisfies the boundary conditions and mass conservation of the lithium-ion diffusion equation.[2,3,9] However, it remains limited in accounting for the time-varying characteristics of battery systems.[2] The Padé approximation method approximates infinite-order analytical solutions as rational transfer functions.[16] The higher the order of the approximate solution, the more accurate it becomes, but it also requires more computation. Since its reduction target needs to be determined at the first step, there should be a trade-off between computation complexity and accuracy, which often needs repetitive experiments that make the order reduction process more cumbersome. In the case of residue grouping methods,[14,15] they expand the theoretical transfer functions of either solid or liquid phases into the sum of an infinite number of first-order transfer functions. Based on fitting in the frequency domain, the integration and grouping of these first-order functions are optimized to a finite-order function. Due to difficulty in solving the liquid phase diffusion equations, finite element methods are required.

The variable temperature presents another challenge for the BMS. The operating temperature range for lithium-ion batteries is typically between −20 °C and 60 °C,[17] with the optimal operating temperature falling between 15 °C and 35 °C.[18] Elevated temperatures can accelerate battery side reactions, leading to material decomposition, the production of flammable gases, and the risk of thermal runaway and self-ignition.[19] Conversely, low temperatures can cause severe

†These authors contributed equally to this work.

‡Corresponding author. E-mail: ximingcheng@163.com

© 2024 Chinese Physical Society and IOP Publishing Ltd

lithium plating, resulting in capacity degradation and internal resistance growth.[17] Therefore, it is essential for battery models to be enhanced by temperature. Battery thermal models can be broadly categorized into numerical computation models, neural network models and lumped thermal parameter models. Numerical computation models include two-dimensional[20] and three-dimensional thermal models.[21–26] The battery's structure, materials and physicochemical properties are used to comprehensively model the temperature distribution inside the battery. However, due to the anisotropic temperature distribution of the battery, the heavy computational burden limits the microelement model's applicability to the BMS. The neural network thermal models[27,28] build mapping among voltage, current and battery temperature using neural networks and provide strong nonlinear approximation. These heuristic models are short of physically meaningful parameters and their performance is seriously influenced by data samples.

Lumped thermal models,[29–35] referred to as equivalent thermal circuit models, simplify the battery's thermal behavior into circuits composed of thermal elements such as heat capacity and thermal resistance. These models usually disregard temperature distribution inside the battery and treat the battery as a uniform temperature whole. On the basis of the number of heat capacity elements, the models are generally categorized into first-order[31–35] and second-order equivalent thermal circuit models.[29,30] These lumped models provide the advantages of clear physical parameter significance, simplicity and low computational costs, quite suitable for real-time applications.

When electrochemical models are coupled with temperature, there are two main aspects to be considered. First, the battery temperature originates from the heat generated by electrochemical reactions, and second, the parameters of the electrochemical model change with temperature.[6,36–38] Compared to isothermal electrochemical models, the thermo-electrochemical models add a heat generation rate equation, the Arrhenius equation, and the Nernst equation.[6] The heat generation rate equation primarily includes the generation of irreversible heat, reversible heat, phase-change heat and mixed heat.[39] Due to the relatively minor impact of phase change and mixed heat, the heat generation rate equation is often simplified to the Bernardi heat generation formula.[29] The Arrhenius equation describes the relationship between temperature and model parameters such as diffusion coefficients and reaction rates. The Nernst equation depicts the variation in the electrode equilibrium potential with temperature.

In this study, we introduce an improved order-reduced method for electrochemical models that can adapt to real-time computation and temperature variation. Based on this, we construct an order-reduced thermal-coupling SPMe model and validate its accuracy under various temperatures and C-rate conditions. We also theoretically demonstrate the inadequacy of traditional models in accommodating real-world operating conditions. The organization of this paper is as follows. Section 2 provides a detailed explanation of the modeling of the SPMe thermal-coupling model, Section 3 presents the experimental setup, Section 4 conducts parameter identification and Section 5 verifies the accuracy of the proposed model.

2. Modeling

2.1. Traditional SPMe model

By using the assumption of uniform reaction in the electrode thickness direction, the SPMe model is simplified from the P2D model.[40] Compared to the SPM model,[41,42] the SPMe model enhanced by the electrolyte dynamics[1,12,43] achieves a better performance balance between accuracy and efficiency. It consists of five sets of equations, primarily including lithium-ion mass transport equations of the solid and liquid phases, liquid-phase potential equations, kinetic equations and terminal voltage equations.

1) Solid-phase lithium-ion mass transport equation

$$\begin{cases} \dfrac{\partial c_{\mathrm{s},\pm}}{\partial t} = \dfrac{D_{\mathrm{s},\pm}}{r^2}\dfrac{\partial}{\partial r}\left(r^2\dfrac{\partial c_{\mathrm{s},\pm}}{\partial r}\right), \quad r \in (0, R_\pm), \\ c_{\mathrm{s},\pm}|_{t=0} = c_{\mathrm{s}0,\pm}, \\ -D_{\mathrm{s},\pm}\dfrac{\partial c_{\mathrm{s},\pm}}{\partial r}\Big|_{r=R_\pm} = 0, \\ -D_{\mathrm{s},\pm}\dfrac{\partial c_{\mathrm{s},\pm}}{\partial r}\Big|_{r=R_\pm} = \mp\dfrac{I}{FAL_\pm a_\pm}, \end{cases} \tag{1}$$

where c denotes the concentration (mol·m^{-3}), the subscript s denotes the solid phase and $\pm$ indicates the positive and negative electrode. t denotes the time coordinate (s), D denotes the diffusion coefficient (m^2·s^{-1}), r denotes the radial coordinate in spherical coordinates (m) and R denotes the radius of spherical particles (m). c_s denotes the initial solid-phase concentration (mol·m^{-3}), I denotes the magnitude of the battery current (A), with a positive sign during discharge and a negative sign during charging, and A denotes the electrode current collector area (m^2). F denotes the Faraday constant (96485 C·mol^{-1}), L denotes thickness, and $a_\pm$ denotes the specific surface area (m^{-1})

$$a_\pm = \frac{3\varepsilon_{\mathrm{s},\pm}}{R_\pm}, \tag{2}$$

where ε denotes the volume fraction.

Arrhenius's formula is used to describe the effect of temperature on the diffusion coefficient, as follows:

$$X = X_{\mathrm{ref}}\exp\left(\frac{E_{\mathrm{a},X}}{R_\mathrm{g}T_{\mathrm{ref}}} - \frac{E_{\mathrm{a},X}}{R_\mathrm{g}T}\right), \tag{3}$$

where X denotes a certain diffusion coefficient, X_{ref} denotes the value of X at the reference temperature T_{ref}, R_g indicates

the gas constant (8.314 J·mol^{-1}·K^{-1}), $E_{a,X}$ denotes the activation energy of parameter X (J·mol^{-1}) and T denotes the temperature (K).

2) Liquid-phase lithium-ion mass transport equation

$$\begin{cases} \varepsilon_{e,\pm}\dfrac{\partial c_{e,\pm}}{\partial t} = \dfrac{\partial}{\partial x}\left(D_{e,\pm}\dfrac{\partial c_{e,\pm}}{\partial x}\right) \mp \dfrac{(1-t_+^0)I}{FAL_\pm}, \\ \varepsilon_{e,sep}\dfrac{\partial c_{e,sep}}{\partial t} = \dfrac{\partial}{\partial x}\left(D_{e,sep}\dfrac{\partial c_{e,sep}}{\partial x}\right), \end{cases} \tag{4}$$

where x denotes the thickness direction coordinate (m), e denotes the liquid phase and t_0^+ denotes the migration coefficient.

The initial and boundary conditions are given by

$$\begin{cases} c_{e,i}|_{t=0} = c_{e0}, \quad i = \pm, \text{sep}, \\ -D_{e,-}\dfrac{\partial c_{e,-}}{\partial x}\Big|_{x=0} = 0, \\ -D_{e,-}\dfrac{\partial c_{e,-}}{\partial x}\Big|_{x=0} = -D_{e,sep}\dfrac{\partial c_{e,sep}}{\partial x}|_{x=L_-}, \\ c_{e,-}|_{x=L_-} = c_{e,sep}|_{x=L_-}, \\ -D_{e,sep}\dfrac{\partial c_{e,sep}}{\partial x}\Big|_{x=L_-+L_{sep}} = -D_{e,+}\dfrac{\partial c_{e,+}}{\partial x}\Big|_{x=L_-+L_{sep}}, \\ c_{e,sep}|_{x=L_-+L_{sep}} = c_{e,+}|_{x=L_-+L_{sep}}, \\ -D_{e,+}\dfrac{\partial c_{e,+}}{\partial x}\Big|_{x=L} = 0. \end{cases} \tag{5}$$

Considering the effect of volume fractions on diffusion coefficients, it is written as

$$D_{e,i} = D_e \times \varepsilon_{e,i}^{\text{Brugg}}, \quad i = \pm, \text{sep}, \tag{6}$$

where Brugg denotes the Bruggeman coefficient. The relationship between the liquid-phase diffusion coefficient and temperature is also described by Eq. (3).

3) Liquid-phase potential equation

$$\begin{aligned} &\phi_e|_{x=L_-+L_{sep}+L_+} - \phi_e|_{x=0} \\ &= -\frac{I}{A}\left(\frac{L_-}{2\kappa_-} + \frac{L_{sep}}{\kappa_{sep}} + \frac{L_+}{2\kappa_+}\right) \\ &\quad + \frac{2R_gT}{F}(1-t_+^0)\ln\frac{c_{e,+}(L,t)}{c_{e,-}(0,t)}, \end{aligned} \tag{7}$$

where ϕ denotes potential (V) and κ denotes the liquid phase conductivity (S·m^{-1}).

4) Kinetic equation

$$\begin{cases} \eta_\pm = \mp\dfrac{2R_gT}{F}\text{arcsinh}\left(\dfrac{I}{2AL_\pm i_{0,\pm}a_\pm}\right), \\ i_{0,\pm} = i_{0\text{ref},\pm}(1-\theta_{ss,\pm})^{0.5}(\theta_{ss,\pm})^{0.5}\left(\dfrac{c_{e0}}{c_{e\text{ref}}}\right)^{0.5}, \\ \theta_{ss,\pm} = \dfrac{c_{ss,\pm}}{c_{s\text{max},\pm}}, \\ \phi_{s,\pm} = \eta_\pm + \phi_{e,\pm} + U_\pm(\theta_{ss,\pm}). \end{cases} \tag{8}$$

In the equation, η denotes overpotential (V), i_{ref} denotes the reference exchange current density (A·m^{-2}), and its temperature dependence is also described by Eq. (3), and θ_{ss} indicates the state of charge (SOC) of the solid-phase spherical particle surface. $c_{e\text{ref}}$ is the reference liquid-phase concentration (mol·m^{-3}), c_{ss} is the surface concentration of spherical particles (mol·m^{-3}) and $c_{s\text{max}}$ is the maximum solid-phase concentration (mol·m^{-3}). $U_\pm$ denotes the electrode equilibrium potential function, and its temperature dependence is stated as follows:

$$U_\pm = U_\pm^{\text{ref}} + (T - T_{\text{ref}})\frac{\partial U_\pm}{\partial T}, \tag{9}$$

where $U_\pm^{\text{ref}}$ is the value of $U_\pm$ under the reference temperature T_{ref} and $\partial U_\pm/\partial T$ is the electrode entropy heat coefficient (V·K^{-1}).

5) Terminal voltage equation

$$V_{\text{cell}} = \phi_{s,+}|_{x=L} - \phi_{s,-}|_{x=0}, \tag{10}$$

where V_{cell} is the output voltage of the model (V).

By combining Eqs. (7) and (8) and considering the current collector, Eq. (10) is expanded as

$$\begin{cases} V_{\text{cell}} = U_+(\theta_{ss,+}) - U_-(\theta_{ss,-}) \\ \qquad - \dfrac{2R_gT}{F}\text{arcsinh}\left(\dfrac{I}{2AL_+ i_{0,+}a_+}\right) \\ \qquad + \dfrac{2R_gT}{F}\text{arcsinh}\left(\dfrac{I}{2AL_- i_{0,-}a_-}\right) \\ \qquad - \dfrac{I}{A}\left(\dfrac{L_-}{2\kappa_-} + \dfrac{L_{sep}}{\kappa_{sep}} + \dfrac{L_+}{2\kappa_+}\right) \\ \qquad + \dfrac{2R_gT}{F}(1-t_+^0)\ln\dfrac{c_{e,+}(L,t)}{c_{e,-}(0,t)}, \\ i_{0,\pm} = i_{0\text{ref},\pm}(1-\theta_{ss,\pm})^{0.5}(\theta_{ss,\pm})^{0.5}\left(\dfrac{c_{e0}}{c_{e\text{ref}}}\right)^{0.5}. \end{cases} \tag{11}$$

2.2. Battery thermal model

The temperature of an object depends on the heat source and the heat transfer pathways. During the charging and discharging processes, the current collectors and the battery tabs have tiny resistance so that the primary heat source inside one battery comes from the Joule heat and reaction heat generated in the jelly. Once heat is generated, it can quickly transfer to the aluminum case tightly contacted to the battery jelly and then dissipate in the air via convective heat exchange. Because aluminum has excellent thermal conductivity, the temperature distribution on the battery case is assumed to be uniform.

A first-order equivalent thermal circuit model is built, as shown in Fig. 1, wherein T_b denotes the average internal temperature of the battery (K), T_s denotes the average surface temperature of the aluminum case (K) and T_{amb} denotes the external ambient temperature (K). q denotes the total heat generation rate inside the battery (W), C_b denotes the heat capacity inside the battery (J/K), R_{in} denotes the average thermal resistance from the battery's interior to the aluminum casing's surface (K/W) and R_{out} denotes the convective heat resistance from the aluminum case to the environment (K/W).

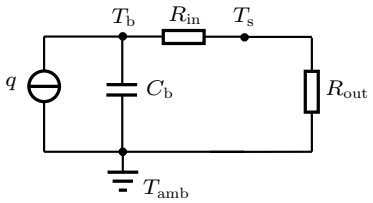


Fig. 1. First-order equivalent thermal circuit model.

The Bernadi heat generation formula is commonly used to obtain the heat generation rate

$$q = I(E_{oc} - V_{cell}) - IT_b\frac{\partial E_{oc}}{\partial T}, \tag{12}$$

where E_{oc} denotes the open circuit voltage (V), a function of SOC, and $\partial E_{oc}/\partial T$ denotes the heat coefficient of battery entropy. During battery discharge, the current I is considered positive, and the heat generation rate of q is also positive. The battery SOC is defined as the ratio of the remaining capacity and rated capacity of the battery

$$\mathrm{SOC} = \left(1 - \frac{Q_{dis}}{Q_{rated}}\right) \times 100\%, \tag{13}$$

where Q_{dis} denotes discharge capacity (Ah) and Q_{rated} denotes the rated capacity (Ah).

In Fig. 1, one part of the heat generated inside the battery is absorbed by the internal components of the battery, leading to an increase in T_b. Another part dissipates into the environment through the internal thermal resistance of R_{in}, and the external thermal resistance of R_{out}.

$$q = C_b\frac{\partial(T_b - T_{amb})}{\partial t} + \frac{T_b - T_s}{R_{in}}, \tag{14}$$

$$\frac{T_b - T_s}{R_{in}} = \frac{T_s - T_{amb}}{R_{out}}, \tag{15}$$

where R_{out} can be further described by Newton's cooling formula

$$R_{out} = \frac{1}{hA_{ex}}, \tag{16}$$

where h denotes the convective heat exchange coefficient ($\mathrm{W{\cdot}m^{-2}{\cdot}K^{-1}}$) and A_{ex} denotes the interface area ($\mathrm{m^2}$).

According to Eq. (15), T_b can be expressed as

$$T_b = \frac{R_{in} + R_{out}}{R_{out}}(T_s - T_{amb}) + T_{amb}. \tag{17}$$

If both R_{in} and R_{out} are known, T_b can only be estimated by measuring two temperatures of T_s and T_{amb}.

2.3. Improved transient polarization voltage drop formula

When the battery either discharges or is charged instantaneously, the transient polarization voltage drop of the traditional SPMe model is calculated as

$$\begin{aligned} U_d(I, \mathrm{SOC}, T) &= IR_\Omega + \frac{2R_gT}{F}\mathrm{arcsinh}\left(\frac{I}{I_{0\mathrm{ref},+}(1-\theta_{ss,+})^{0.5}(\theta_{ss,+})^{0.5}}\right) \\ &\quad + \frac{2R_gT}{F}\mathrm{arcsinh}\left(\frac{I}{I_{0\mathrm{ref},-}(1-\theta_{ss,-})^{0.5}(\theta_{ss,-})^{0.5}}\right), \end{aligned} \tag{18}$$

where

$$\begin{cases} I_{0\mathrm{ref},\pm} = 2AL_\pm i_{0\mathrm{ref},\pm}\left(\dfrac{c_{e0}}{c_{\mathrm{eref}}}\right)^{0.5}, \\ R_\Omega = \dfrac{1}{A}\left(\dfrac{L_-}{2\kappa_-} + \dfrac{L_{sep}}{\kappa_{sep}} + \dfrac{L_+}{2\kappa_+}\right), \\ \theta_{ss,\pm} = \mathrm{SOC} \times \theta_{s0,\pm} + (1 - \mathrm{SOC}) \times \theta_{s1,\pm}. \end{cases} \tag{19}$$

However, this formula tends to produce considerable discrepancies from the actual battery response. This issue will be discussed in the following sections.

2.3.1. Problem of traditional transient polarization voltage drop formula under different currents

When one battery maintains a constant temperature T and a full charge, its parameters of R_l, T, $I_{0\mathrm{ref},+}(1-\theta_{ss,+})^{0.5}(\theta_{ss,+})^{0.5}$ and $I_{0\mathrm{ref},-}(1-\theta_{ss,-})^{0.5}(\theta_{ss,-})^{0.5}$ in Eq. (18) are all definite values. In this case, there are two constants of K_T and $I_{T0,\pm}$ defined as follows:

$$\begin{cases} K_T = 2R_gT/F, \\ I_{T0,\pm} = I_{0\mathrm{ref},\pm}(1-\theta_{ss,\pm})^{0.5}(\theta_{ss,\pm})^{0.5}. \end{cases} \tag{20}$$

Consequently, the transient polarization voltage drop at SOC=100% can be expressed by

$$U_d = IR_l + K_T\mathrm{arcsinh}(I/I_{T0,+}) + K_T\mathrm{arcsinh}(I/I_{T0,-}). \tag{21}$$

Herein, a transient internal resistance is noted by

$$\begin{aligned} R_d &= \frac{U_d}{I} \\ &= R_l + \frac{K_T\mathrm{arcsinh}(I/I_{T0,+}) + K_T\mathrm{arcsinh}(I/I_{T0,-})}{I}. \end{aligned} \tag{22}$$

There is an inference that R_d decreases with the increase in I. The fact that the partial derivative of R_d with respect to I is less than zero needs to be demonstrated. It is given by

$$\begin{aligned} \frac{\partial R_d}{\partial I} &= \frac{1}{I_{T0,+}I}\left[\frac{1}{\sqrt{(I/I_{T0,+})^2+1}} - \frac{\mathrm{arcsinh}\,(I/I_{T0,+})}{I/I_{T0,+}}\right] \\ &\quad + \frac{1}{I_{T0,-}I}\left[\frac{1}{\sqrt{(I/I_{T0,-})^2+1}} - \frac{\mathrm{arcsinh}\,(I/I_{T0,-})}{I/I_{T0,-}}\right] < 0, \\ &\quad I > 0. \end{aligned} \tag{23}$$

Due to

$$\lim_{I\to 0}\frac{\partial R_d}{\partial I} = 0, \tag{24}$$

only the following inequality needs to be confirmed:

$$\begin{aligned} &\frac{1}{\sqrt{x^2+1}} - \frac{\mathrm{arcsinh}\,(x)}{x} = \frac{x - \sqrt{x^2+1}\,\mathrm{arcsinh}\,(x)}{x\sqrt{x^2+1}} < 0, \\ &x > 0, \end{aligned} \tag{25}$$

which is

$$F(x) = x - \sqrt{x^2+1}\,\mathrm{arcsinh}\,(x) < 0, \quad x > 0, \tag{26}$$

considering that

$$F(0) = 0, \tag{27}$$

only the following inequality needs to be proved:

$$F'(x) = -x\,\mathrm{asinh}\,(x)/\sqrt{x^2+1} < 0, \quad x > 0. \tag{28}$$

And so Eq. (28) is evidently valid.

Figure 2 shows the transient internal resistance variation with current for the battery at full charge and a temperature of 30 °C. As observed in this figure, the transient internal resistance fluctuates below 5 A. This may be attributed to external factors impacting the transient polarization voltage at lower currents. Beyond 5 A, the transient internal resistance remains relatively stable, at around 6.5 mΩ. This indicates that the transient internal resistance does not follow the monotonous decrease pattern with increasing current as assumed in the SPMe model. This problem is that the traditional transient polarization voltage drop formula cannot accord with experimental data. A possible reason for this discrepancy may originate from the hypothesis of uniform flux of the SPMe model contradicting the micro-behavior of practical batteries.

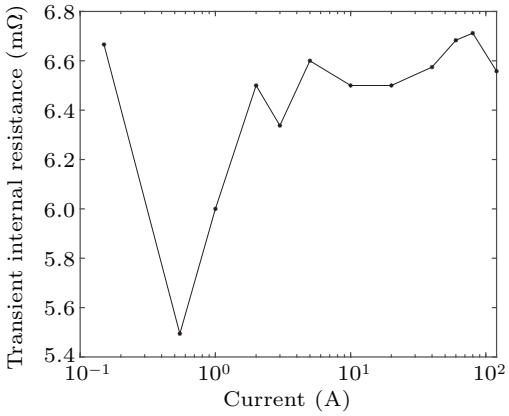


Fig. 2. Relationship between transient internal resistance and current.

2.3.2. Problem of traditional transient polarization voltage drop formula under different SOCs

When the temperature and current remain constant, the transient polarization value in the SPMe model changes with the discharge capacity of the battery, and the relationship can be expressed as follows:

$$U_\mathrm{d} = U_l + K_T h(K_+, \theta_{\mathrm{ss},+}) + K_T h(K_-, \theta_{\mathrm{ss},-}), \tag{29}$$

where parameters $U_l = IR_l$, $K_T = 2R_\mathrm{g}T/F$ and $K_\pm = I/I_{0\mathrm{ref},\pm}$ are both constant at uniform temperature. The function $h(\cdot)$ means

$$h(K,x) = \mathrm{arcsinh}\frac{K}{\sqrt{x(1-x)}}, \quad K > 0, \quad 0 < x < 1. \tag{30}$$

The following context will explain the inadequacy of Eq. (29) for the transient polarization voltage under different SOC for the experimental battery. Table 1 lists the transient polarization voltages for different SOCs of the battery at discharge currents of 15 A at 10 °C, 20 °C and 30 °C. It is evident from the data that the polarization voltage varies similarly at all three temperatures. Specifically, when the SOC is greater than 46%, the transient polarization voltage remains relatively stable, whereas it increases if the SOC is less than 46%. Assuming that seven parameters of U_l, K_T, $K_\pm$, $\theta_{\mathrm{s0},\pm}$ and $\theta_{\mathrm{s1},\pm}$ enable Eq. (29) to fit the transient polarization voltage data at 10 °C, it can serves as an example to illustrate the inadequacy of Eq. (30) in fitting the transient polarization voltage under various SOCs.

First, the nature of the function $h(K,x)$ in Eq. (30) concerning the variable x needs to be investigated. Figure 3 illustrates the variation curve of $h(K,x)$ concerning x. Obviously, $h(K,x)$ monotonically decreases for $x < 0.5$, and monotonically increases for $x > 0.5$, with its minimum value occurring at $x = 0.5$. In addition, it is notable that the rate of monotonic decrease of $h(K,x)$ becomes slower as $x \in (0, 0.5)$, while the rate of monotonic increase becomes faster as $x \in (0.5, 1)$.

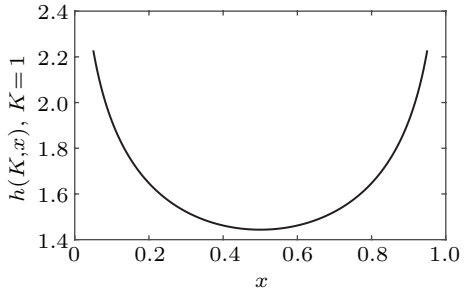


Fig. 3. The curve of function $h(K,x)$ at $K = 1$.

Table 1. Transient polarization voltages of different SOCs at an excitation current of 15 A.

SOC (%)	100.0	93.24	86.5	79.7	73.0	66.2	59.5
$T = 10$ °C (mV)	119	120	120	119	120	121	118
$T = 20$ °C (mV)	91	92	92	92	92	93	93
$T = 30$ °C (mV)	73	73	73	73	73	73	73
SOC (%)	52.7	45.9	39.2	32.4	25.7	18.9	12.2
$T = 10$ °C (mV)	118	120	123	137	146	158	178
$T = 20$ °C (mV)	93	93	96	99	104	114	133
$T = 30$ °C (mV)	73	73	74	77	78	81	89

In other words, the first derivative of $h(K,x)$ is equal to 0 at $x=0.5$, and the second derivative of $h(K,x)$ remains non-negative for $x\in(0,1)$, that is,

$$\frac{\partial h(K,x)}{\partial x}\Big|_{x=0.5}=\frac{K(2x-1)}{2x(1-x)\sqrt{x(1-x)+K^2}}\Big|_{x=0.5}=0, \tag{31}$$

$$\frac{\partial^2 h(K,x)}{\partial x^2}=\frac{K\left(4K^2(x-0.5)^2+K^2+8x(1-x)\left((x-0.5)^2+0.25\right)\right)}{4x^2(1-x)^2(x(1-x)+K^2)^{3/2}}>0. \tag{32}$$

Equations (31) and (32) are evidently valid.

If the initial SOC of the negative electrode $\theta_{s0,-}$ is less than 0.5, i.e., $\theta_{ss,-}|_{SOC=100\%}<0.5$, $\theta_{ss,-}$ will continuously decrease as the battery SOC exceeds 46%. Thus, the parameter of $K_T h(K,\theta_{ss,-})$ of the negative electrode gradually increases. However, the overall transient polarization voltage remains unchanged. This indicates that the parameter of $K_T h(K_+,\theta_{ss,+})$ of the positive electrode gradually decreases. Furthermore, $\theta_{ss,+}$ gradually increases with the decrease in SOC, indicating that $\theta_{ss,+}|_{SOC<46\%}$ is less than 0.5. From 100% to 93.2% of SOC, the change in transient polarization voltage could be neglected, leading to the following equation:

$$\begin{aligned}&h(K_+,\theta_{ss,+})|_{SOC=100\%}-h(K_+,\theta_{ss,+})|_{SOC=93.2\%}\\=\;&h(K_-,\theta_{ss,-})|_{SOC=93.2\%}-h(K_-,\theta_{ss,-})|_{SOC=100\%}.\end{aligned} \tag{33}$$

From 93.2% to 86.5% of SOC, the change of transient polarization voltage could be almost negligible, leading to the following equation:

$$\begin{aligned}&h(K_+,\theta_{ss,+})|_{SOC=93.2\%}-h(K_+,\theta_{ss,+})|_{SOC=86.5\%}\\=\;&h(K_-,\theta_{ss,-})|_{SOC=86.5\%}-h(K_-,\theta_{ss,-})|_{SOC=93.2\%}.\end{aligned} \tag{34}$$

Using Lagrange's mean value theorem, there are $\theta_{1,\pm}$ and $\theta_{2,\pm}$ confirming that

$$\begin{cases}\theta_{1,+}\in(\theta_{ss,+}|_{SOC=100\%},\theta_{ss,+}|_{SOC=93.2\%}),\\ \theta_{1,-}\in(\theta_{ss,+}|_{SOC=93.2\%},\theta_{ss,+}|_{SOC=100\%}),\\ \theta_{2,+}\in(\theta_{ss,+}|_{SOC=93.2\%},\theta_{ss,+}|_{SOC=86.5\%}),\\ \theta_{2,-}\in(\theta_{ss,-}|_{SOC=86.5\%},\theta_{ss,+}|_{SOC=93.2\%}),\\ 0.5>\theta_{2,+}>\theta_{1,+}>0,\quad 0<\theta_{2,-}<\theta_{1,-}<0.5,\end{cases} \tag{35}$$

resulting in

$$\begin{cases}\mathrm{d}\theta_+\dfrac{\partial h(K_+,x)}{\partial x}\Big|_{x=\theta_{1,+}}=h(K_+,\theta_{ss,+})|_{SOC=100\%}\\ \qquad\qquad -h(K_+,\theta_{ss,+})|_{SOC=93.2\%},\\ \mathrm{d}\theta_-\dfrac{\partial h(K_-,x)}{\partial x}\Big|_{x=\theta_{1,-}}=h(K_-,\theta_{ss,-})|_{SOC=100\%}\\ \qquad\qquad -h(K_-,\theta_{ss,-})|_{SOC=93.2\%},\\ \mathrm{d}\theta_+\dfrac{\partial h(K_+,x)}{\partial x}\Big|_{x=\theta_{2,+}}=h(K_+,\theta_{ss,+})|_{SOC=93.2\%}\\ \qquad\qquad -h(K_+,\theta_{ss,+})|_{SOC=86.5\%},\\ \mathrm{d}\theta_-\dfrac{\partial h(K_-,x)}{\partial x}\Big|_{x=\theta_{2,-}}=h(K_-,\theta_{ss,-})|_{SOC=93.2\%}\\ \qquad\qquad -h(K_-,\theta_{ss,-})|_{SOC=86.5\%},\end{cases} \tag{36}$$

where

$$\begin{cases}\mathrm{d}\theta_+=\theta_{ss,+}|_{SOC=100\%}-\theta_{ss,+}|_{SOC=93.2\%}\\ \qquad=\theta_{ss,+}|_{SOC=93.2\%}-\theta_{ss,+}|_{SOC=86.5\%}<0,\\ \mathrm{d}\theta_-=\theta_{ss,-}|_{SOC=100\%}-\theta_{ss,-}|_{SOC=93.2\%}\\ \qquad=\theta_{ss,-}|_{SOC=93.2\%}-\theta_{ss,-}|_{SOC=86.5\%}>0,\end{cases} \tag{37}$$

and because $\partial h(K,x)/\partial x$ increases monotonically as $x\in(0,0.5)$, remaining negative, the following equation can be obtained from Eqs. (35)–(37):

$$\begin{cases}(h(K_+,\theta_{ss,+})|_{SOC=93.2\%}-h(K_+,\theta_{ss,+})|_{SOC=86.5\%})\\ >(h(K_+,\theta_{ss,+})|_{SOC=100\%}-h(K_+,\theta_{ss,+})|_{SOC=93.2\%})>0,\\ h(K_-,\theta_{ss,-})|_{SOC=93.2\%}-h(K_-,\theta_{ss,-})|_{SOC=100\%}\\ >h(K_-,\theta_{ss,-})|_{SOC=86.5\%}-h(K_-,\theta_{ss,-})|_{SOC=93.2\%}>0.\end{cases} \tag{38}$$

Combining Eqs. (33) and (38), the following inequality can be obtained:

$$\begin{aligned}&h(K_+,\theta_{ss,+})|_{SOC=93.2\%}-h(K_+,\theta_{ss,+})|_{SOC=86.5\%}\\>\;&h(K_-,\theta_{ss,-})|_{SOC=86.5\%}-h(K_-,\theta_{ss,-})|_{SOC=93.2\%}.\end{aligned} \tag{39}$$

Obviously, Eq. (39) contradicts Eq. (34), indicating that Eq. (29) cannot explain the phenomenon where the transient polarization voltage remains basically constant at SOC $>46\%$. It can be demonstrated that, no matter what the SOC value is, the θ_{ss} is given by 0.5. The above contradiction still exists. If we neglect $K_\pm$, the transient polarization voltage would remain nearly constant with SOC, but by observing Table 1, it is evident that the transient polarization voltage increases as the SOC decreases below 46%. This suggests a strong relationship between the transient polarization voltage and SOC. In summary, Eq. (29) is not suitable for fitting the transient polarization voltage data of the experimental battery at different SOC values.

2.3.3. A novel fitted transient polarization voltage drop formula

Considering the two issues related to current and SOC variations, an improvement has been made for the transient polarization voltage drop formula to conform to experimental data. To create the relationship between the transient polarization voltage, SOC, and temperature, inspiration is drawn from

the Arrhenius equation, leading to the following modification:

$$U_{\rm d}(I,{\rm SOC},T)=I\times R_{\rm ref}({\rm SOC})\times\exp\left(\frac{E_{\rm aR}}{R_{\rm g}T}-\frac{E_{\rm aR}}{R_{\rm g}T_{\rm ref}}\right), \quad (40)$$

where $R_{\rm ref}$ (SOC) denotes the transient internal resistance function varying with SOC at the reference temperature $T_{\rm ref}$ (K). $E_{\rm aR}$ denotes the activation energy of the transient internal resistance (J).

It can be observed that when the ambient temperature remains stable at 30 °C and the battery is full, the transient internal resistance is about 6.5 mΩ, as shown in Fig. 2. In contrast, the transient internal resistance in Table 1 is around 4.96 mΩ. The reason for this difference is that the previous data were collected nearly three months before the latter, during which time the battery aged, resulting in increased internal resistance. To adapt to the internal resistance changes caused by aging, Eq. (40) needs further refinement. Specifically, when the battery starts discharging at an initial SOC of $\rm SOC_1$ and an initial temperature of T_1, with an excitation current of I_1, a transient polarization voltage of $U_{\rm d}=U_{\rm d1}$ is measured at the first second, and the subsequent transient polarization voltage during discharge is produced by

$$\begin{aligned}&U_{\rm d,ol}(I,{\rm SOC},T)\\&=I\times R_{\rm ref}({\rm SOC})\times\exp\left(\frac{E_{\rm aR}}{R_{\rm g}T}-\frac{E_{\rm aR}}{R_{\rm g}T_{\rm ref}}\right)\\&\quad\times\frac{U_{\rm d1}}{U_{\rm d}(I_1,{\rm SOC}_1,T_1)}.\end{aligned} \quad (41)$$

Hence, the terminal voltage expression of the SPMe model is improved by

$$\begin{aligned}V_{\rm cell}&=U_+(\theta_{\rm ss,+})|_{x=L}-U_-(\theta_{\rm ss,-})|_{x=0}-U_{\rm d,ol}(I,{\rm SOC},T)\\&\quad+\frac{2R_{\rm g}T}{F}(1-t_+^0)\ln\frac{c_{\rm e,+}(L,t)}{c_{\rm e,-}(0,t)}.\end{aligned} \quad (42)$$

2.4. Order reduction of solid-phase lithium-ion mass transport equation

Under constant current conditions, the time-domain analytical solution of the solid mass transport equation can be given by[44]

$$\begin{aligned}\bar{c}_{\rm s,\pm}&=\pm\frac{I}{3FAL_\pm\varepsilon_{\rm s,\pm}}\left\{3t+\frac{5r^2-3R_\pm^2}{10R_\pm^2}\tau_\pm\right.\\&\quad\left.-\frac{2R_\pm}{r}\left[\sum_{m=1}^{\infty}\frac{\sin(\lambda_m r/R)}{\sin(\lambda_m)}\tau_{\pm,m}\exp\left(-\frac{t}{\tau_{\pm,m}}\right)\right]\right\},\end{aligned} \quad (43)$$

where

$$\bar{c}_{\rm s,\pm}=c_{\rm s,\pm}-c_{\rm s0,\pm}, \quad (44)$$

$$\tau_\pm=\frac{R_\pm^2}{D_{\rm s,\pm}}, \quad (45)$$

$$\tau_{\pm,m}=\frac{\tau_\pm}{\lambda_m^2},\quad m=1,2,3,\ldots, \quad (46)$$

where λ_m denotes the mth positive root of the equation $\lambda=\tan\lambda$. In addition, $\tau_\pm$ satisfies

$$\lim_{m->\infty}\sum_{i=1}^{m}\tau_{\pm,i}=\frac{\tau_\pm}{10}. \quad (47)$$

Since only the surface concentration of spherical particles has a direct effect on the model output, the analytical solution is given by

$$\begin{aligned}\bar{c}_{\rm ss,\pm}&=\pm\frac{I}{3FAL_\pm\varepsilon_{\rm s,\pm}}\\&\quad\times\left\{3t+2\sum_{m=1}^{\infty}\tau_{\pm,m}\left[1-\exp\left(-\frac{t}{\tau_{\pm,m}}\right)\right]\right\}.\end{aligned} \quad (48)$$

Equation (48) is truncated to an mth order function. Then we have

$$\begin{aligned}\bar{c}_{\rm ss,\pm}&=\pm\frac{I}{3FAL_\pm\varepsilon_{\rm s,\pm}}\\&\quad\times\left\{3t+2\sum_{m=1}^{M}\tau_{\pm,m}\left[1-\exp\left(-\frac{t}{\tau_{\pm,m}}\right)\right]\right\}.\end{aligned} \quad (49)$$

However, the final value of Eq. (49) differs from that of Eq. (48), and after compensation, we obtain

$$\begin{aligned}\bar{c}_{\rm ss,\pm}&=\pm\frac{I}{3FAL_\pm\varepsilon_{\rm s,\pm}}\left\{3t+2\sum_{m=1}^{M-1}\tau_{\pm,m}\left[1-\exp\left(-\frac{t}{\tau_{\pm,m}}\right)\right]\right.\\&\quad\left.+\left(\frac{\tau_\pm}{5}-2\sum_{m=1}^{M-1}\tau_{\pm,m}\right)\left[1-\exp\left(-\frac{t}{\tau_{\pm,M}}\right)\right]\right\}.\end{aligned} \quad (50)$$

Equation (48) is conducted using the Laplace transform and divided by I/s to yield the transfer function of the current I to $\bar{c}_{\rm ss,\pm}$ as follows:

$$\begin{aligned}G_{\rm s,\pm}&=\pm\frac{1}{3FAL_\pm\varepsilon_{\rm s,\pm}}\left\{\frac{3}{s}+\frac{1}{5}\sum_{m=1}^{M-1}\frac{\tau_{\pm,m}}{\tau_{\pm,m}s+1}\right.\\&\quad\left.+\frac{\lambda_M^2}{5}\left(1-10\sum_{m=1}^{M-1}\frac{1}{\lambda_m^2}\right)\frac{\tau_{\pm,M}}{\tau_{\pm,M}s+1}\right\}.\end{aligned} \quad (51)$$

According to Eqs. (3) and (45), the relationship between solid-phase time constant $\tau_{\pm,m}$ and T can be described by

$$\tau_{\pm,m}=\frac{\tau_{\rm ref,\pm}}{\lambda_m^2}\exp\left(\frac{E_{\rm as,\pm}}{R_{\rm g}T}-\frac{E_{\rm as,\pm}}{R_{\rm g}T_{\rm ref}}\right), \quad (52)$$

where $\tau_{\rm ref,\pm}$ denotes the value of $\tau_\pm$ under the temperature of $T_{\rm ref}$. $E_{\rm as,\pm}$ denotes the corresponding activation energy.

To create a balance between numerical model accuracy and computational efficiency, a third-order transfer function is approximated by truncating Eq. (51):

$$\begin{aligned}G_{\rm s,\pm}&=\pm\frac{1}{3FAL_\pm\varepsilon_{\rm s,\pm}}\left\{\frac{3}{s}+\frac{1}{5}\frac{\tau_{\pm,1}}{\tau_{\pm,1}s+1}+\frac{1}{5}\frac{\tau_{\pm,1}}{\tau_{\pm,1}s+1}\right.\\&\quad\left.+\left(\frac{\lambda_3^2}{5}-\frac{2\lambda_3^2}{\lambda_1^2}-\frac{2\lambda_3^2}{\lambda_2^2}\right)\frac{\tau_{\pm,3}}{\tau_{\pm,3}s+1}\right\}.\end{aligned} \quad (53)$$

Herein, $\theta_{\rm s0,\pm}$ and $\theta_{\rm s1,\pm}$ mean the solid-phase charge states of the positive and negative electrodes at full charge and full

discharge of the battery, respectively. Then, the battery capacity of $Q_{\rm bat}$ can be defined by

$$Q_{\rm bat} = \pm FAL_{\pm}\varepsilon_{{\rm s},\pm}c_{{\rm smax},\pm}(\theta_{{\rm s1},\pm} - \theta_{{\rm s0},\pm}). \tag{54}$$

Combining Eqs. (8), (53) and (54), the solid-phase surface state of charge $\theta_{{\rm ss},\pm}$ can be written as

$$G_1 = \frac{\theta_{{\rm s1},\pm} - \theta_{{\rm s0},\pm}}{3Q_{\rm bat}}\left\{\frac{3}{s} + \frac{1}{5}\frac{\tau_{\pm,1}}{\tau_{\pm,1}s+1} + \frac{1}{5}\frac{\tau_{\pm,1}}{\tau_{\pm,1}s+1} + \left(\frac{\lambda_3^2}{5} - \frac{2\lambda_3^2}{\lambda_1^2} - \frac{2\lambda_3^2}{\lambda_2^2}\right)\frac{\tau_{\pm,3}}{\tau_{\pm,3}s+1}\right\}. \tag{55}$$

2.5. Order reduction of liquid-phase lithium-ion mass transport equation

Using our previously published work,[45] the analytical solutions to the liquid-phase mass transport Eqs. (4)–(6) under constant current conditions are given by

$$\bar{c}_{\rm e} = Ip_0(x)\tau_{{\rm e},m} + I\sum_{i=1}^{\infty} p_m(x)\tau_{{\rm e},m}\left[1 - \exp\left(-\frac{t}{\tau_{{\rm e},m}}\right)\right], \tag{56}$$

where

$$\begin{cases} \bar{c}_{\rm e} = c_{\rm e} - c_{\rm e0}, \\ \sum\limits_{i=1}^{\infty} p_i(x) = p_0(x), \end{cases} \tag{57}$$

where p_i denotes coefficients and $\tau_{{\rm e},i}$ denotes time constants. However, the parameters of Eq. (56) are only valid under isothermal conditions. Thus, the relationship between these parameters and temperature is created, as shown in the following sections.

From Eqs. (3) and (6), the relationship between the liquid-phase diffusion coefficient and temperature is given by

$$D_{{\rm e},i} = D_{{\rm eref},i}\exp\left(\frac{E_{\rm ae}}{R_{\rm g}T_{\rm ref}} - \frac{E_{\rm ae}}{R_{\rm g}T}\right), \quad i = \pm, {\rm sep}, \tag{58}$$

where $D_{{\rm eref},i}$ denotes the value of $D_{{\rm e},i}$ at the reference temperature $T_{\rm ref}$, and $E_{\rm ae}$ denotes the corresponding activation energy. Substituting Eq. (58) into the liquid-phase mass transport Eqs. (4)–(6), the liquid-phase mass transport equations at the reference temperature $T_{\rm ref}$ can be yielded by

$$\begin{cases} \varepsilon_{{\rm e},\pm}\dfrac{\partial c_{{\rm e},\pm}}{\partial\left[\exp\left(\dfrac{E_{\rm ae}}{R_{\rm g}T} - \dfrac{E_{\rm ae}}{R_{\rm g}T_{\rm ref}}\right)t\right]} = \dfrac{\partial}{\partial x}\left(D_{{\rm e},\pm}\dfrac{\partial c_{{\rm e},\pm}}{\partial x}\right) \mp \dfrac{(1-t_+^0)}{FAL_{\pm}}\dfrac{I}{\exp\left(\dfrac{E_{\rm ae}}{R_{\rm g}T} - \dfrac{E_{\rm ae}}{R_{\rm g}T_{\rm ref}}\right)}, \\ \varepsilon_{\rm e,sep}\dfrac{\partial c_{\rm e,sep}}{\partial\left[\exp\left(\dfrac{E_{\rm ae}}{R_{\rm g}T} - \dfrac{E_{\rm ae}}{R_{\rm g}T_{\rm ref}}\right)t\right]} = \dfrac{\partial}{\partial x}\left(D_{\rm e,sep}\dfrac{\partial c_{\rm e,sep}}{\partial x}\right). \end{cases} \tag{59}$$

Equations (5) and (6) remain unchanged. Since Eqs. (5) and (6) are the analytical solutions to the equations under constant current conditions, the analytical solution to Eq. (59) under constant current conditions is stated by

$$\bar{c}_{\rm eref} = \frac{I\tau_{{\rm e},m}}{\exp\left(\dfrac{E_{\rm ae}}{R_{\rm g}T} - \dfrac{E_{\rm ae}}{R_{\rm g}T_{\rm ref}}\right)}\left\{p_0(x) + \sum_{m=1}^{\infty} p_m(x)\left[1 - \exp\left(-\frac{\exp\left(\dfrac{E_{\rm ae}}{R_{\rm g}T} - \dfrac{E_{\rm ae}}{R_{\rm g}T_{\rm ref}}\right)t}{\tau_{{\rm e},m}}\right)\right]\right\}. \tag{60}$$

Then, the time constant $\tau_{{\rm eref},m}$ under $T_{\rm ref}$ can be obtained by

$$\tau_{{\rm eref},m} = \tau_{{\rm e},m}\exp\left(\frac{E_{\rm ae}}{R_{\rm g}T_{\rm ref}} - \frac{E_{\rm ae}}{R_{\rm g}T}\right). \tag{61}$$

From Eqs. (60) and (61), it can be determined that the parameters of p_m of Eq. (56) do not vary with temperature, while the relationship between $\tau_{{\rm e},m}$ and temperature is expressed by

$$\tau_{{\rm e},m} = \tau_{{\rm eref},m}\exp\left(\frac{E_{\rm ae}}{R_{\rm g}T} - \frac{E_{\rm ae}}{R_{\rm g}T_{\rm ref}}\right). \tag{62}$$

Similarly, the order-reduced technique is also applied to the solid-phase reduction process and the mth-order reduced transfer function from current to liquid-phase concentration can be given by

$$G_{\rm e} = \sum_{m=1}^{M-1} p_m\frac{\tau_{{\rm e},m}}{\tau_{{\rm e},m}s+1} + \left(p_0 - \sum_{m=1}^{M-1} p_m\right)\frac{\tau_{{\rm e},M}}{\tau_{{\rm e},M}s+1}. \tag{63}$$

For the liquid-phase mass transport equation, the determination of each order transfer function relies on nine parameters, which makes it difficult to solve in practice. Herein, a first-order transfer function approximation is employed to obtain

$$G_{\rm e}(x) = \frac{p_0(x)\tau_{\rm e}}{\tau_{\rm e}s+1}, \tag{64}$$

where $\tau_{\rm e}$ denotes an abbreviation of $\tau_{{\rm e},1}$.

Assuming that the positive and negative poles of the liquid phase are symmetric, we have

$$\begin{cases} c_{{\rm e},+}(L,t) = c_{\rm e0} - \bar{c}_{\rm e}(0), \\ c_{{\rm e},-}(0,t) = c_{\rm e0} + \bar{c}_{\rm e}(0). \end{cases} \tag{65}$$

Then, the concentration polarization voltage drop of the liquid phase in the model output voltage is written as

$$\frac{2R_{\rm g}T}{F}(1-t_+^0)\ln\frac{c_{{\rm e},+}(L,t)}{c_{{\rm e},-}(0,t)} = \frac{2R_{\rm g}T}{F}(1-t_+^0)\ln\frac{1-\theta_{\rm e}}{1+\theta_{\rm e}}, \tag{66}$$

where θ_e denotes the normalized excess liquid concentration

$$\theta_e = \frac{\bar{c}_e(0)}{c_{e0}}. \tag{67}$$

Finally, the transfer function from the current I to θ_e can be expressed by

$$G_2 = \frac{1}{Q_e}\frac{\tau_e}{\tau_e s+1}, \tag{68}$$

where

$$Q_e = \frac{c_{e0}}{p_0(0)}. \tag{69}$$

2.6. Order-reduced thermal-coupling SPMe model

Based on the above derivation, an order-reduced thermal-coupling SPMe model can be constructed. The output voltage equation of this model can be stated by

$$\begin{aligned} V_{\text{cell}} = {} & U_+(\theta_{\text{ss},+})|_{x=L} - U_-(\theta_{\text{ss},-})|_{x=0} - U_{\text{d,ol}}(I,\text{SOC},T) \\ & + \frac{2R_gT}{F}(1-t_+^0)\ln\frac{1-\theta_e}{1+\theta_e}. \end{aligned} \tag{70}$$

Herein, the transfer functions of $\theta_{\text{ss},\pm}$ and θ_e with respect to current I are expressed by Eqs. (55) and (68). The specific form of $U_{\text{d,ol}}(I,\text{SOC},T)$ is given by Eq. (41). The temperature T denotes the average temperature inside the battery and can be calculated using Eq. (17),

$$T = T_b = \frac{R_{\text{in}}+R_{\text{out}}}{R_{\text{out}}}(T_s - T_{\text{amb}}) + T_{\text{amb}}. \tag{71}$$

The needed identification parameters of the order-reduced SPMe thermal-coupling model are tabulated in Table 2.

Table 2. The model parameters.

Thermal model parameters	Transient polarization voltage parameters	Equilibrium potential parameter	Solid-phase polarization parameters	Liquid-phase polarization parameter
$R_{\text{in}}, R_{\text{out}}$	$R_{\text{ref}}(\text{SOC}), E_{\text{aR}}$	$U_\pm^{\text{ref}}, \partial U_\pm/\partial T, \theta_{\text{s0},\pm}, \theta_{\text{s1},\pm}$	$\tau_\pm, E_{\text{as},\pm}$	$Q_e, \tau_e, E_{\text{ae}}, t_+^0$

3. Experimental detials

3.1. Battery sample

The battery sample is an aluminum-shell prismatic wound-type ternary lithium-ion battery. Due to their convenient pack design, aluminum-shell prismatic batteries are commonly used in electric vehicles.[46–48] The battery specification is listed in Table 3 and its shape is shown in Figs. 4(a)–4(c). In Fig. 4(b), the copper foil indicates the location where one temperature sensor is bonded to the battery surface.

Table 3. The battery parameters.

Parameters	Values
Rated capacity (Ah)	37
Battery weight (g)	816
Battery size (mm)	$148\times27\times92.4$
Cut-off voltage (V)	2.8–4.2
Rated voltage (V)	3.65
Optimal operating temperature (°C)	15–35



Fig. 4. The battery shape: (a) top view; (b) front view; (c) side view.

3.2. Experimental platform

The experimental setup was built as illustrated in Fig. 5. Figure 5(a) shows the experimental equipment and instrument, including a chamber, a charger and a FLUKE data logger.

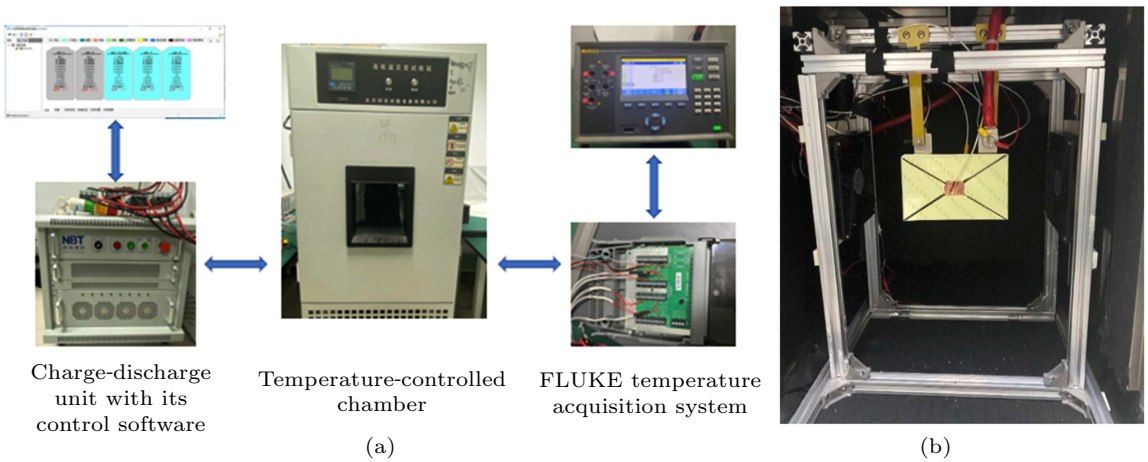


Fig. 5. Test bench: (a) equipment and instrument; (b) battery sample displacement.

Figure 5(b) provides the displacement of the sample battery inside the chamber. The battery rack is made of aluminum and integrated with fans on both sides. There are four temperature sensors, three each attached to the positive tab, negative tab, surface central point, and one hung in the ambient air, respectively.

This chamber can be used to set up a constant temperature environment for the sample battery, the temperature of which can be modified by using its control panel. Each fan speed can change with its supply voltage for variable convective heat exchange on the battery surface. The control software on the upper computer is used to operate the charger for variable current and voltage excitation to the sample battery. Simultaneously, the battery current and voltage can be recorded on the upper computer. The FLUKE data logger is used to record battery temperature, current, voltage and ambient temperature.

3.3. Test profiles

Three values, 10 °C, 20 °C and 30 °C, are set for the chamber temperature, respectively. There are five current values of 10 A, 20 A, 40 A, 80 A and 120 A for battery discharge. In addition, there are three dynamic charge–discharge cycles of the worldwide harmonized light vehicles test cycle (WLTC), the new European driving cycle (NEDC), and the dynamic stress test (DST) conducted on the sample battery, respectively. Figure 6 illustrates the dynamic profiles used in the experiments, where discharge and charge current are positive and negative, respectively.

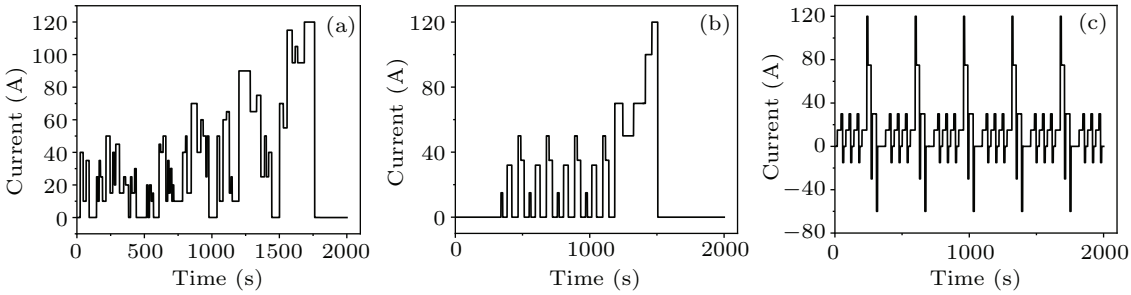


Fig. 6. The profile of dynamic conditions: (a) WLTC; (b) NEDC; (c) DST.

For convenient description in subsequent sections, there is an abbreviation to denote the combination of the working conditions. For example, the drive cycle of DST conducted at 20 °C is denoted as 20dDST. The constant discharge current of 40 A and the temperature at 20 °C is denoted as 20d40A.

4. Parameter identification

4.1. Parameter identification of the thermal model

4.1.1. Identification methods

In the case of the battery cell sealed by the aluminum shell, it is difficult to directly measure the internal temperature of $T_{\rm in}$. Equations (14) and (15) can be combined to eliminate $T_{\rm in}$.

$$q = C_{\rm b}\left(1+\frac{R_{\rm in}}{R_{\rm out}}\right)\frac{{\rm d}T_{\rm ss}}{{\rm d}t}+\frac{T_{\rm ss}}{R_{\rm out}}, \tag{72}$$

where $T_{\rm ss}$ denotes the surface excess temperature

$$T_{\rm ss} = \frac{T_{\rm s}-T_{\rm amb}}{R_{\rm out}}. \tag{73}$$

The Laplace transform is conducted on Eq. (72) to produce the transfer function from q to $T_{\rm ss}$

$$G(s) = \frac{T_{\rm ss}(s)}{q(s)} = R_{\rm out}\frac{1}{\tau s+1}, \tag{74}$$

where $T_{\rm ss}(s)$ and $q(s)$ denote the Laplace transform of $T_{\rm ss}$ and q, respectively. τ denotes the time constant

$$\tau = C_{\rm b}(R_{\rm out}+R_{\rm in}). \tag{75}$$

The internal thermal resistance of $R_{\rm in}$ and thermal capacitance of $C_{\rm b}$ are supposed constant. By setting up different external convective environments, the external thermal resistance of $R_{\rm out,1}$ and the time constant of τ_1 can be determined. Consequently, $R_{\rm in}$ can be derived based on Eq. (75)

$$\begin{cases} R_{\rm in} = \dfrac{\tau R_{\rm out,1}-\tau_1 R_{\rm out}}{\tau_1-\tau}, \\ C_{\rm b} = \dfrac{\tau-\tau_1}{R_{\rm out}-R_{\rm out,1}}. \end{cases} \tag{76}$$

The backward Euler algorithm is employed to discretize the time-continuous thermal system at a step of 1 s. The optimization objective function is designed to minimize the mean squared error (MSE) between the predicted surface temperature and its actual measured values. The genetic algorithm is applied to estimate thermal parameters.

4.1.2. Measurements of the open-circuit voltage and entropy coefficient

The $E_{\rm oc}$ is a function of the battery SOC. Figure 7(a) illustrates the current–voltage curve to identify the open-circuit voltage at a temperature of 20 °C. Figure 7(b) shows the curve fitted with the extracted open-circuit voltage points in Fig. 7(a). The fitted expression for $E_{\rm oc}$ is given by

$$E_{\rm oc}({\rm SOC}) = \frac{0.595}{{\rm e}^{57.0x-56.9}+1}-\frac{0.148}{{\rm e}^{18.2-21.6x}+1}$$

$$-\frac{0.996}{e^{0.304-4.59x}+1}+3.94. \tag{77}$$

The entropy coefficient denotes the rate of the open-circuit voltage with respect to temperature. It is necessary for the battery at each set SOC to be rested at room temperature over 8 h until the terminal voltage is stable. Then, the chamber is adjusted to a predesigned temperature. After that, the relationship between the open-circuit voltage and temperature can be observed, as shown in Fig. 8. Using tiny scales, linear functions are used to fit the relationship between terminal voltage and battery temperature. Herein, the line slope denotes the battery's entropy coefficient as listed in Table 4.

Table 4. Battery entropy coefficients at different SOCs.

SOC (%)	100	73	46	19
Entropy coefficient ($V\cdot K^{-1}$)	-4.6×10^{-5}	5.8×10^{-6}	1×10^{-4}	-8.3×10^{-5}

It can be seen from Fig. 8 and Table 4 that the temperature has a tiny influence on the open-circuit voltage. For instance, the maximum entropy coefficient listed in Table 4 is 1×10^{-4} $V\cdot K^{-1}$, indicating that a temperature change of 10 °C results in only a 1 mV variation in the open-circuit voltage.

The generation rate of irreversible heat is much greater than that of reversible heat. When a battery is discharging, the difference between the open-circuit voltage and the terminal voltage can result in a significant increase in the irreversible heat generation rate (HGR). However, as shown in Table 4, the reversible HGR fluctuates between positive and negative values, partially offsetting heat production. Furthermore, when the battery current increases, the ratio between the irreversible HGR and the reversible HGR can increase. Hence, the reversible HGR could be ignored and Eq. (12) is concisely rewritten as

$$q = I(E_{oc} - V_{cell}). \tag{78}$$

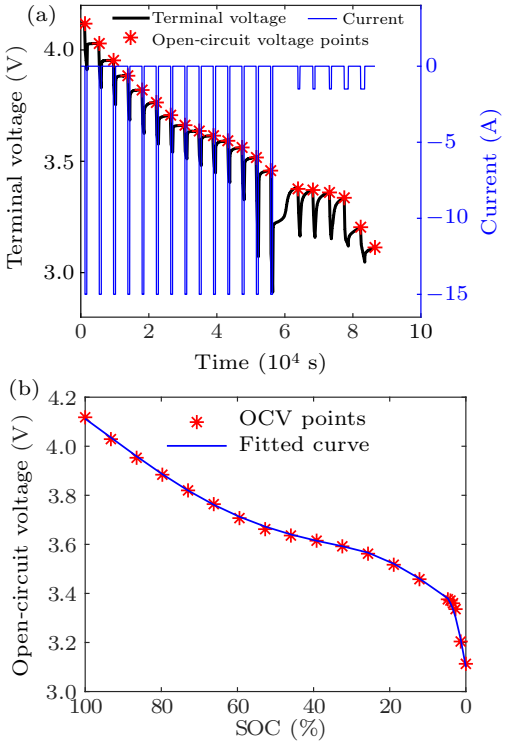


Fig. 7. The curves of the open-circuit voltage: (a) test curve; (b) fitted curve.

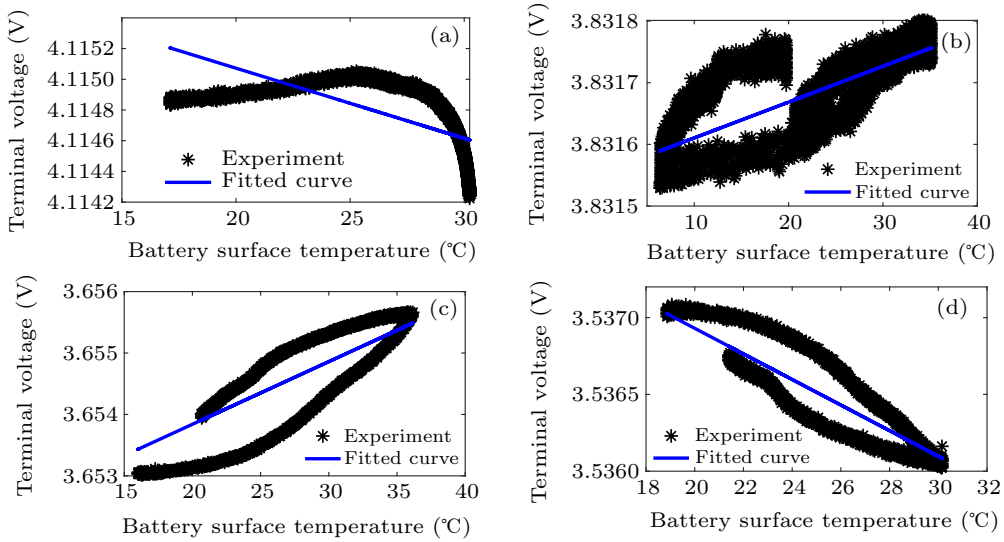


Fig. 8. Battery voltage versus temperature: (a) SOC = 100%; (b) SOC = 73%; (c) SOC = 46%; (d) SOC = 19%.

4.1.3. Identification of thermophysical property parameters

The convective heat exchange on the battery surface can be regulated by changing the voltage connected to the fans. There are two voltages of 0 V and 12 V powered to the fans. The curves of the HGR and temperature rise are shown in Fig. 9. Figures 9(a) and 9(c) show the heat rates and fitted curves, calculated using Eq. (78), under the conditions of 0 V and 12 V, respectively. Figures 9(b) and 9(d) display the curves of measurements and models of the temperature rise. As il-

lustrated in Figs. 9(a) and 9(c), the HGR gradually tends to become stable during charging and discharging, as the battery temperature increases and approaches stability. The internal resistance can change synchronously with temperature, subsequently directly influencing the HGR. Comparing Figs. 9(b) and 9(d), the temperature is more stable when the fan voltage is 0 V. This may be attributed to the airflow generated by the fan at 12 V interfering with the airflow produced inside the chamber, causing slight disturbances and minor temperature fluctuations.

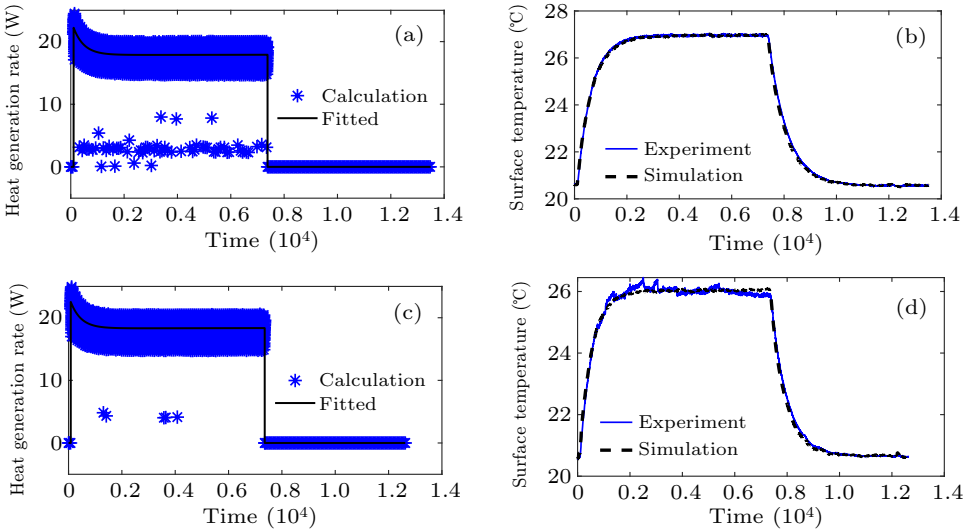


Fig. 9. Heat generation rate and temperature rise with different fan voltages: (a) 0 V-HGR; (b) 0 V-temperature rise; (c) 12 V-HGR; (d) 12 V-temperature rise.

The transfer functions of HGR with respect to the battery temperature under two convective conditions are expressed by

$$\begin{cases} G_{0\ \mathrm{V}} = \dfrac{0.3362}{s/(1.5\times10^{-3})+1}, \\ G_{12\ \mathrm{V}} = \dfrac{0.2712}{s/(1.8\times10^{-3})-3+1}. \end{cases} \tag{79}$$

Combining Eqs. (74) and (76), there are two thermophysical property parameters of the battery that can be given by

$$\begin{cases} R_{\mathrm{in}} = 0.0538\ \mathrm{K\cdot W^{-1}}, \\ C_{\mathrm{b}} = 1709.4\ \mathrm{J\cdot K^{-1}}. \end{cases} \tag{80}$$

At the same time, the two external thermal resistances can also be given by

$$\begin{cases} R_{\mathrm{out},0\ \mathrm{V}} = 0.3362\ \mathrm{K\cdot W^{-1}}, \\ R_{\mathrm{out},12\ \mathrm{V}} = 0.2712\ \mathrm{K\cdot W^{-1}}. \end{cases} \tag{81}$$

It is possible for the external thermal resistance to vary under different operating conditions. Supposing that the internal thermal resistance and thermal capacitance remain constant, the external thermal resistance is only related to the environmental chamber temperature. Therefore, the chamber temperature is set at 10 °C, 20 °C and 30 °C, respectively. A constant current of 40 A is used to discharge the sample battery in order to correct the external thermal resistance. The identification results are presented in Table 5. Thus, the model predictions of battery temperature are plotted in Fig. 10. It can be seen from the results that the presented thermal model achieves a good performance.

Table 5. External thermal resistance identified at different temperatures.

Temperature (°)	10	20	30
External thermal resistance ($\mathrm{K\cdot W^{-1}}$)	0.4721	0.4818	0.3790

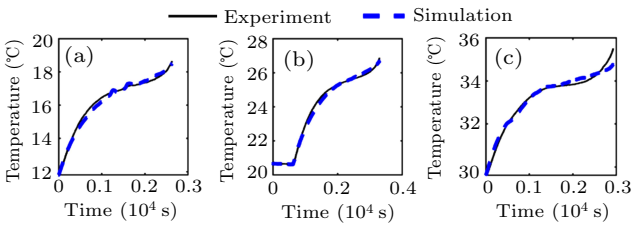


Fig. 10. Prediction results of battery surface temperature at different temperatures: (a) 10d40A; (b) 20d40A; (c) 30d40A.

4.2. Parameter identification of transient polarization voltage drop

In Eq. (40), T_{ref} is set by 293.15 K so that the fitting of the data in Table 1 is given by

$$\begin{cases} R_{\mathrm{ref}}(\mathrm{SOC}) = \left(\dfrac{9.19}{\mathrm{e}^{11.7\mathrm{SOC}-0.482}+1} - \dfrac{2.8}{\mathrm{e}^{1.78-0.484\mathrm{SOC}}+1} + 6.69\right)\times10^{-3}, \quad T_{\mathrm{ref}} = 293.15, \\ E_{\mathrm{aR}} = 19284. \end{cases} \tag{82}$$

The fitting results, as shown in Fig. 11, indicate that the overall fitting curves align with their evolution trend of the polarization voltage. It is noteworthy that there is a slight increase in the fitting error at a temperature of 30 °C and SOC < 20%. This may be attributed to the relatively faster decrease in internal resistance of the battery at higher temperatures.

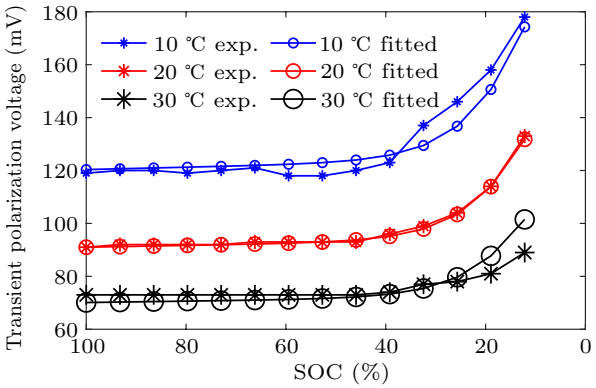


Fig. 11. Transient polarization voltage fitting curves at 15 A excitation current.

4.3. Parameter identification of equilibrium potential

To obtain the parameters of $U_{\pm}^{\mathrm{ref}}$ and $\partial U_{\pm}/\partial T$ relative to the positive and negative electrode equilibrium potential functions, the open-circuit voltage of E_{oc} should be analyzed. When the battery is reset, its terminal voltage of V_{cell} is equal to E_{oc},

$$E_{\mathrm{oc}}(\mathrm{SOC}) = U_{+}(\theta_{\mathrm{ss},+}) - U_{-}(\theta_{\mathrm{ss},-}). \tag{83}$$

The relationship between $\theta_{\mathrm{ss},\pm}$ and SOC is expressed by

$$\theta_{\mathrm{ss},\pm} = \mathrm{SOC} \times \theta_{\mathrm{s0},\pm} + (1-\mathrm{SOC}) \times \theta_{\mathrm{s1},\pm}, \tag{84}$$

where $\theta_{\mathrm{s0},\pm}$ and $\theta_{\mathrm{s1},\pm}$ denote the electrode SOC when fully charged and fully discharged, respectively. At a fully charge state, most of the lithium ions are located inside the negative electrode and a few are inside the positive electrode. Then, we have

$$\begin{cases} 0 < \theta_{\mathrm{s1},-} < \theta_{\mathrm{s0},-} < 1, \\ 0 < \theta_{\mathrm{s0},+} < \theta_{\mathrm{s1},+} < 1. \end{cases} \tag{85}$$

In addition, according to Eq. (83), the relationship between $\partial U_{\pm}/\partial T$ and entropy coefficient $\partial E_{\mathrm{oc}}/\partial T$ can be produced by

$$\frac{\partial E_{\mathrm{oc}}}{\partial T} = \frac{\partial U_{+}}{\partial T} - \frac{\partial U_{-}}{\partial T}. \tag{86}$$

Thereby, the difference in the electrode equilibrium potentials is approximately equivalent to the change in the open-circuit voltage when the battery SOC decreases. The magnitude of the entropy coefficient for the positive and negative electrodes is generally less than 1 mV/K in the literatures.[6,49] Hence, the influence of the entropy coefficient is disregarded in the model.

$$U_{\pm} = U_{\pm}^{\mathrm{ref}}. \tag{87}$$

The E_{oc} at 20 °C is used to determine $U_{\pm}$. Due to the confidentiality of the lithium-ion battery materials by the battery manufacturer, we suppose that the negative electrode material of this sample battery is graphite. Therefore, its equilibrium potential function can be obtained by[50]

$$\begin{aligned} &U_{-}(\theta_{\mathrm{ss},-}) \\ &= 0.3824\mathrm{e}^{-665.8\theta_{\mathrm{ss},-}} - 0.03131\tan^{-1}(25.59\theta_{\mathrm{ss},-} - 4.099) \\ &\quad - 0.009434\tan^{-1}(32.49\theta_{\mathrm{ss},-} - 15.74) \\ &\quad - 1.0\mathrm{e}^{39.42\theta_{\mathrm{ss},-}-41.92} + 0.8493\mathrm{e}^{-61.79\theta_{\mathrm{ss},-}} + 0.1493. \end{aligned} \tag{88}$$

Similarly, the $\theta_{\mathrm{s0},\pm}$ and $\theta_{\mathrm{s1},\pm}$ of the battery electrodes can be given by[50]

$$\begin{cases} \theta_{\mathrm{s0},-} = 0.801, \quad \theta_{\mathrm{s1},-} = 0.043, \\ \theta_{\mathrm{s0},+} = 0.360, \quad \theta_{\mathrm{s1},+} = 0.956. \end{cases} \tag{89}$$

When combined with Eq. (83), the positive equilibrium potential function can be expressed by

$$\begin{aligned} U_{+}(\theta_{\mathrm{ss},+}) &= E_{\mathrm{oc}}(\mathrm{SOC}) + U_{-}(\theta_{\mathrm{ss},-}) \\ &= \frac{0.481}{\mathrm{e}^{90.4\theta_{\mathrm{ss},+}-86.4}+1.0} - \frac{0.911}{\mathrm{e}^{3.36-8.62\theta_{\mathrm{ss},+}}+1.0} \\ &\quad + \frac{0.0767}{\mathrm{e}^{30.1\theta_{\mathrm{ss},+}-25.3}+1.0} \\ &\quad + 4.04, \quad \theta_{\mathrm{ss},+} \in (0.360, 0.956). \end{aligned} \tag{90}$$

Figure 12 shows the curves of E_{oc}, U_{+}, U_{-} and the reference positive electrode equilibrium voltage $U_{+}[\mathrm{Ref}]$.[50] At high SOC, the curve of U_{+} almost resembles that of $U_{+}[\mathrm{Ref}]$. At low SOC, they have significant differences. This discrepancy may be attributed to the potential differences in the chemical composition of the NCM electrode between the experimental battery and reference sample. However, except for the curve of U_{-}, the other three curves for characterizing the potential of the positive electrode tend to be closer.

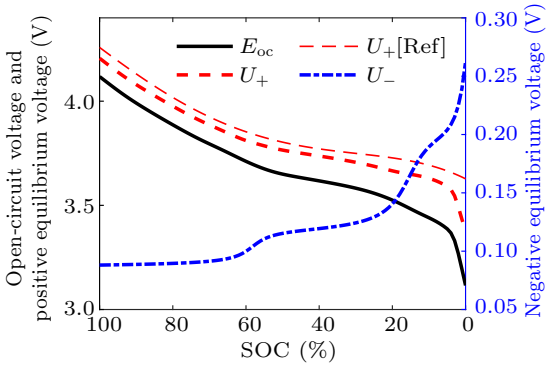


Fig. 12. Diagrams of E_{oc}, U_{+}, U_{-} and $U_{+}[\mathrm{Ref}]$.

4.4. Solid–liquid phase polarization parameter identification

Regarding the liquid-phase polarization process, θ_e should lie within the range of $(-1, 1)$ to make Eq. (42) meaningful. For a constant current discharge, $\theta_e > 0$. From Eq. (68), the expression of θ_e can be expressed by a function of time t

$$\theta_e(t) = \frac{I\tau_e}{Q_e}\left(1-\exp\left(-t/\tau_e\right)\right), \quad t \in [0, t_L], \tag{91}$$

wherein t_L denotes the discharge duration. It is evident that $\theta_e(t)$ increases as t increases. And $\theta_e(t)$ is less than 1 for $t \in [0, t_L]$. Then, there is a constraint that Q_e should satisfy the following inequality:

$$Q_e \geq I\tau_e\left(1-\exp\left(-t_L/\tau_e\right)\right). \tag{92}$$

The relationship between Q_e and τ_e can be confirmed using the data in Table 6, wherein the durations of constant current discharges at three different temperatures of 10 °C, 20 °C and 30 °C are listed. As the temperature increases and discharge rates decrease, the discharge durations gradually become longer. However, it is noteworthy that at 20 °C, the discharge duration at 120 A constant current is longer than at 30 °C under the same conditions. It may be that the operating conditions of 30 °C at 120 A constant discharging causes some internal damage to the battery.

The relationship between the minimum values of Q_e and τ_e is shown in Fig. 13, wherein the curve of "max" denotes the maximum value of Q_e corresponding to τ_e at these three temperatures. It is denoted as $fQ_{e\min}(\tau_e)$. Consequently, an inequality can be yielded by

$$Q_e(\tau_e) \geq fQ_{e\min}(\tau_e). \tag{93}$$

Table 6. Summary of constant current discharge durations (s).

Current	10 A	20 A	40 A	80 A	120 A
10 °C	12012	5558	2627	1163	301
20 °C	12323	5837	2677	1299	711
30 °C	13120	6367	2925	1376	443

The data acquired from three operating conditions of 10d40A, 20d40A and 30d40A are applied to extract the solid–liquid phase polarization parameters. Herein, the MSE of the terminal voltage is selected for the optimization objective. The optimization problem can be described by

$$\begin{cases} \min\ f_{\mathrm{Err}}(\tau_{\mathrm{ref},\pm}, E_{\mathrm{as},\pm}, \tau_{\mathrm{eref}}, E_{\mathrm{ae}}, Q_e) \\ = \mathrm{MSE}_{10\mathrm{d}40\mathrm{A}} + \mathrm{MSE}_{20\mathrm{d}40\mathrm{A}} + \mathrm{MSE}_{30\mathrm{d}40\mathrm{A}}, \\ \text{s.t.}\quad \tau_{\mathrm{ref},\pm}, E_{\mathrm{as},\pm}, \tau_{\mathrm{eref}}, E_{\mathrm{ae}}, Q_e > 0, \\ \quad Q_e \geq fQ_{e\min}(\tau_e), \end{cases}, \tag{94}$$

where $\mathrm{MSE}_{10\mathrm{d}40\mathrm{A}}$, $\mathrm{MSE}_{20\mathrm{d}40\mathrm{A}}$ and $\mathrm{MSE}_{30\mathrm{d}40\mathrm{A}}$ denote the MSE values between the model-simulated voltages and actual voltages. The model-simulated voltages are calculated using Eq. (42).

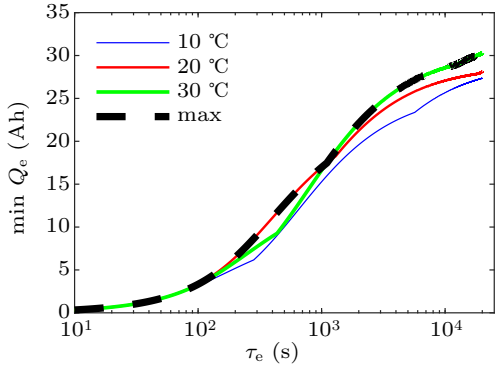


Fig. 13. The relationship between the minimum Q_e values and τ_e at different temperatures.

The reference temperature of T_{ref} is 20 °C. The genetic algorithm is conducted to obtain the values of the solid–liquid phase polarization parameters as follows:

$$\begin{cases} E_{\mathrm{as},-} = 77783,\ E_{\mathrm{a},+} = 8461.3,\ E_{\mathrm{ae}} = 37497, \\ \tau_{\mathrm{ref},-} = 6033.7,\ \tau_{\mathrm{ref},+} = 2594.3,\ \tau_{\mathrm{eref}} = 8745.5, \\ Q_e = 29.54, \end{cases} \tag{95}$$

where the relationship between the solid–liquid time constant and temperature is stated by

$$\begin{cases} \tau_-(T) = 6033.7\exp\left[77783(1/T - 1/T_{\mathrm{ref}})/R_g\right], \\ \tau_+(T) = 2594.3\exp\left[8461.3(1/T - 1/T_{\mathrm{ref}})/R_g\right], \\ \tau_e(T) = 8745.5\exp\left[37497(1/T - 1/T_{\mathrm{ref}})/R_g\right]. \end{cases} \tag{96}$$

The ion migration coefficient of t_+^0 is obtained from Refs. [51,52], the value of which is equal to 0.3633. It should be noted that the model solvers used in this section and the next section are MATLAB-based.

5. Results and discussion

There are two parts, including battery temperature estimation and the SPMe thermal-coupling model, to be validated using the test data of the sample battery. It has been demonstrated that the proposed order-reduced electrochemical model has good capability in computing the solid-phase SOC and the liquid-phase lithium-ion concentration, the results of which are close to the finite element analysis.[44,45] Therefore, if the model voltage approximates the experimental values, the polarization voltage calculation can be confirmed.

5.1. Estimation of internal battery temperature

The solid–liquid phase time constants, concentration polarization potential, and other physical quantities in the SPMe model are functions of the average temperature of T inside the battery. Thus, it is necessary to estimate T first. Using Eq. (71), T can be calculated after T_s, T_{amb}, R_{in} and R_{out} are either measured or extracted, respectively. Figures 14 and 15 give the results of the estimated battery temperature under various working conditions.

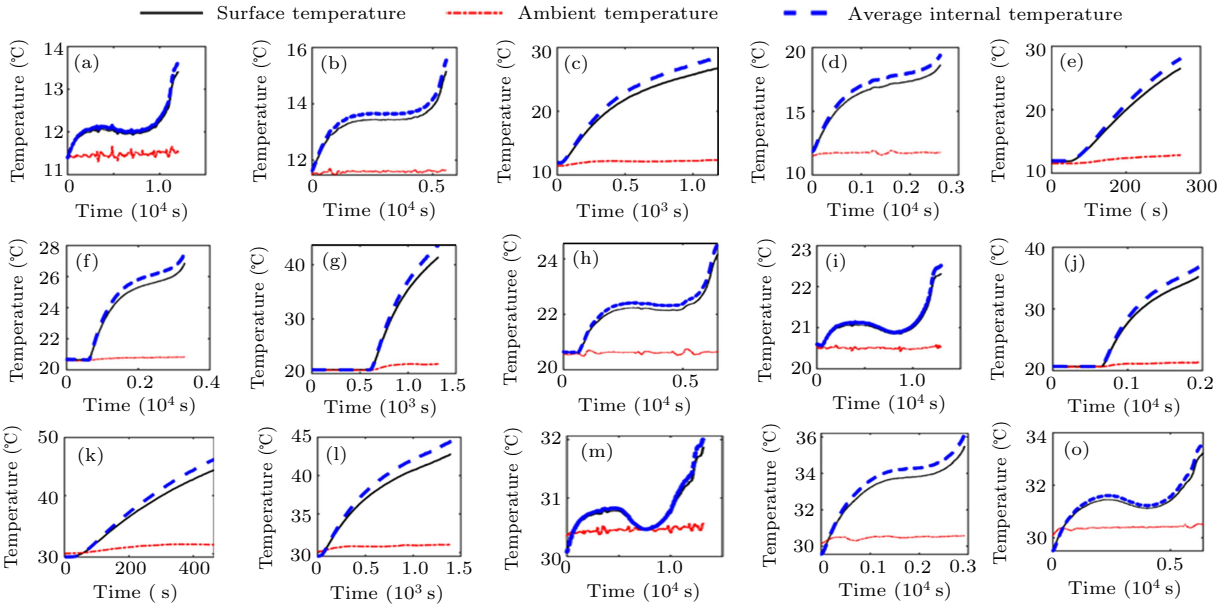


Fig. 14. Estimation results of the internal average temperature of the battery under constant current conditions: (a) 10d10A; (b) 10d20A; (c) 10d40A; (d) 10d80A; (e) 10d120A; (f) 20d10A; (g) 20d20A; (h) 20d40A; (i) 20d80A; (j) 20d120A; (k) 30d10A; (l) 30d20A; (m) 30d40A; (n) 30d80A; (o) 30d120A.

Here, every estimated curve behaves consistently, slightly higher than the battery surface temperature, and their temperature difference is not greater than 1.5 °C. As the battery temperature increases, these *D*-values also grow. The battery surface directly exchanges heat with its ambient air, dissipates heat more rapidly than the battery's internal materials, and leads to a lower surface temperature. The reason for the relatively small *D*-values is that the internal thermal resistance of the battery is so low that it transfers heat efficiently.

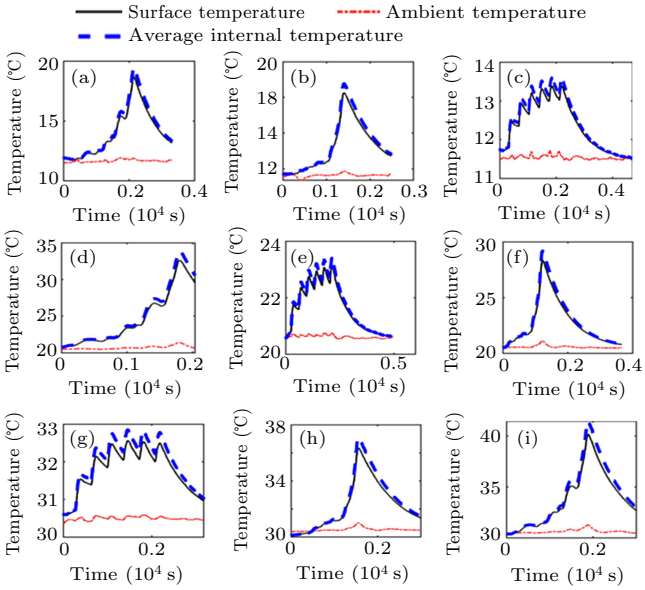


Fig. 15. Estimation results of the average internal temperature of the battery under dynamic conditions: (a) 10dWLTC; (b) 10dNEDC; (c) 10dDST; (d) 20dWLTC; (e) 20dNEDC; (f) 30dDST; (g) 30dWLTC; (h) 30dNEDC; (i) 30dDST.

5.2. Results analysis for thermal-coupling SPMe

Figure 16 presents a comparison between the simulation and experimental results for the SPMe model under 15 constant current discharge conditions (10 A, 20 A, 40 A, 80 A and 120 A) at temperatures of 10 °C, 20 °C and 30 °C, respectively. It also provides the corresponding error curves. Figure 17 illustrates the comparison between the simulation and experimental results for the SPMe model under nine dynamic discharge conditions (WLTC, NEDC and DST) at temperatures of 10 °C, 20 °C and 30 °C, respectively. It also shows the model error curves. Table 7 lists statistical data obtained through the use of root mean square error (RMSE) and mean absolute error (MAE) for the SPMe model excited by the above 24 conditions, the information of which is provided in Fig. 18.

In Fig. 16, under various constant current conditions, it can be seen from the results that the errors between the simulation and experimental results are small in the early to mid-discharge phases and become larger in the later discharge phases. For example, in the case of the constant current discharges of 10 A, 20 A and 40 A, the voltage errors in the early to mid-phase are almost less than 20 mV, while the errors rapidly increase over 100 mV in the later phase, even up to 250 mV. This may be attributed to severe and inconsistent polarization effects on the sample battery while deeply discharging. However, excited by similar constant current at 25 °C, the proposed model produced better accuracy compared to the conventional model.[53] At an 80 A constant discharge, the model errors initially increase and then decrease, the values of which are not greater than 80 mV. In the case of a 120 A constant discharge, the model errors generally tend to increase, possibly originating from increasing uneven distribution of ions at this long-time high-rate discharge.

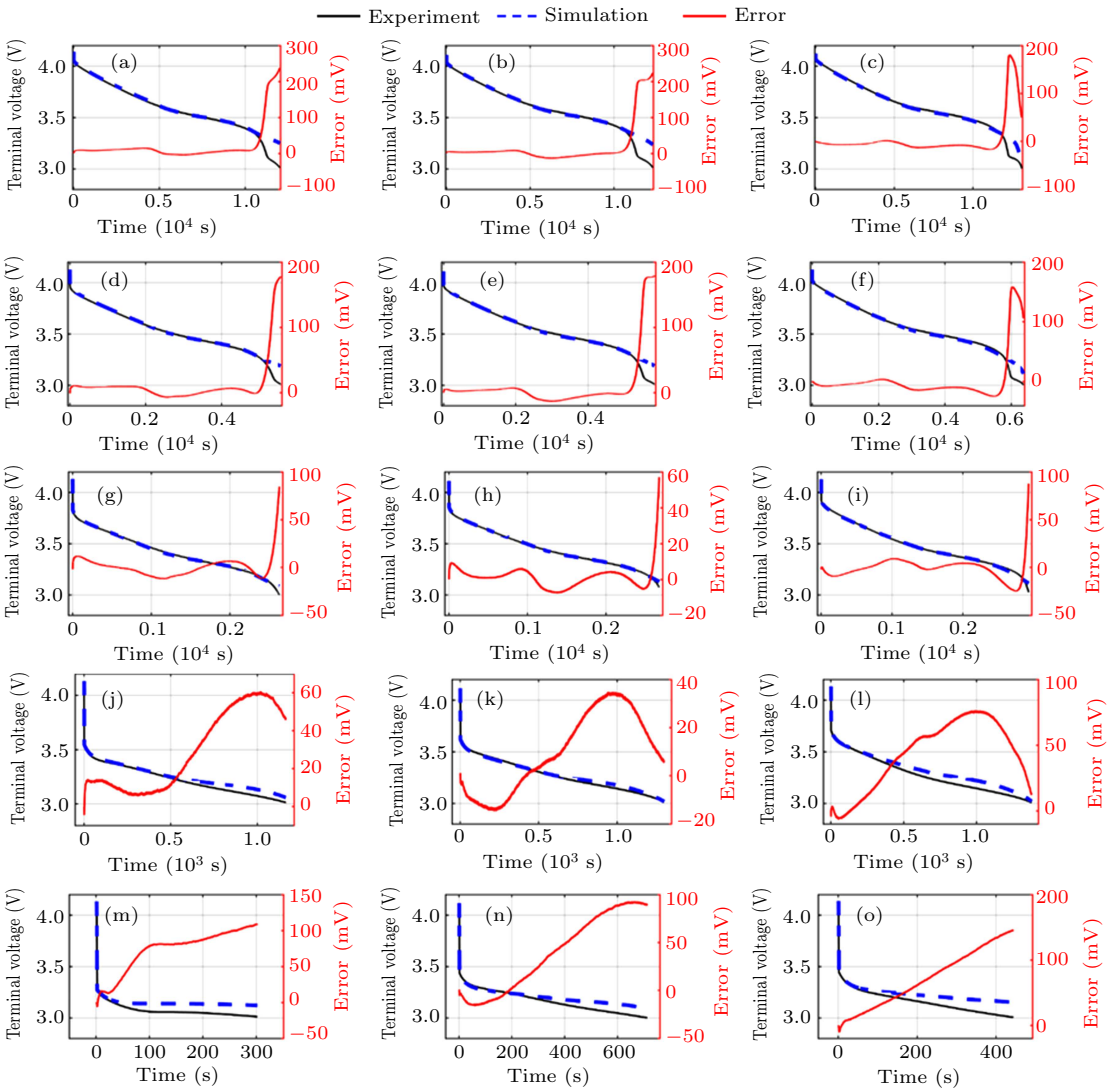


Fig. 16. SPMe calculation results under constant current conditions: (a) 10d10A; (b) 20d10A; (c) 30d10A; (d) 10d20A; (e) 20d20A; (f) 30d20A; (g) 20d40A; (h) 20d40A; (i) 30d40A; (j) 10d80A; (k) 20d80A; (l) 30d80A; (m) 10d120A; (n) 20d120A; (o) 30d120A.

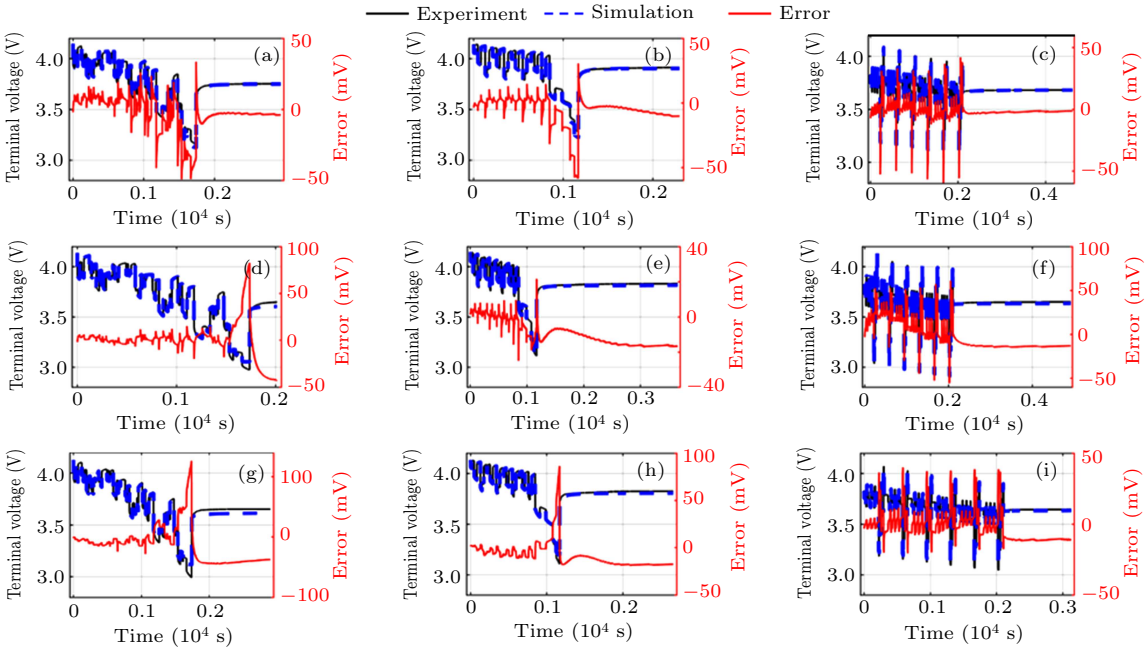


Fig. 17. SPMe calculation results under dynamic conditions: (a) 10dWLTC; (b) 10dNEDC; (c) 10dDST; (d) 20dWLTC; (e) 20dNEDC; (f) 30dDST; (g) 30dWLTC; (h) 30dNEDC; (i) 30dDST.

Table 7. The error of SPMe (mV).

	10d10A	10d20A	10d40A	10d80A	10d120A	10dWLTC	10dNEDC	10dDST
RMSE	56.8	35.6	11.0	35.8	78.9	12.3	12.2	6.4
MAE	238.0	177.9	84.6	60.4	109.5	49.2	58.6	59.6
	20d10A	20d20A	20d40A	20d80A	20d120A	20dWLTC	20dNEDC	20dDST
RMSE	60.8	43.9	6.8	19.0	54.9	18.9	11.7	15.0
MAE	224.2	178.9	57.1	34.5	92.3	82.5	25.0	61.2
	30d10A	30d20A	30d40A	30d80A	30d120A	30dWLTC	30dNEDC	30dDST
RMSE	40.7	39.1	10.7	50.3	83.6	32.9	15.7	10.7
MAE	180.9	158.9	87.7	76.0	145.9	126.1	86.5	40.0

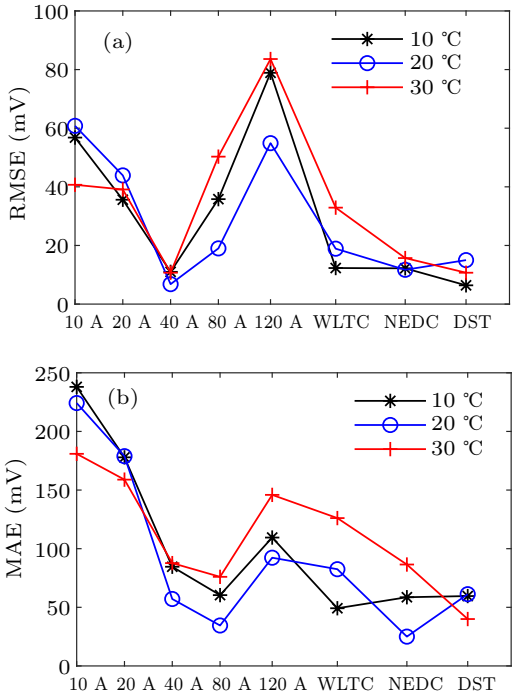


Fig. 18. The overall error curves of the proposed SPMe model: (a) RMSE; (b) MAE.

In Fig. 17, under the three dynamic conditions of WLTC, NEDC and DST, most voltage errors are less than 20 mV. However, the local maximum error points often coincide at moments of rapid current changes, such as around 1000 s and 1600 s in the case of NEDC and WLTC, respectively. This may result from substantial polarization effects on the internal resistance caused by a sudden current.

As shown in Table 7 and Fig. 18, the model errors under dynamic conditions are smaller than those under constant current conditions. The average value of RMSE under dynamic conditions is 15 mV, while it is 42 mV under constant current conditions. This *D*-value may result from the cumulative polarization effects under constant current excitation on the sample battery. In addition, there are relatively large errors observed at the end of discharge under the constant current conditions of 10 A and 20 A. This can be attributed to a low-rate current leading to a deep discharge of the sample battery, as shown in Figs. 16(a)–16(f).

In summary, the results obtained under 24 different operating conditions demonstrate that the proposed SPMe thermal-coupling model has a good estimation accuracy of battery terminal voltage.

6. Conclusion

This study presents an order-reduced thermal-electrochemical SPMe model validated by the use of test data. First, a first-order equivalent thermal circuit model is constructed to estimate the battery's average temperature. Second, through theoretical derivations, it is demonstrated that the transient polarization voltage drop formula of the traditional SPMe model is not suitable for various current excitation. Then, a new empirical formula is proposed and can be used at different temperatures. Finally, a third-order transfer function and a first-order transfer function are created to characterize the solid and liquid phases of battery electrodes, respectively, reducing orders of the SPMe model. Moreover, the thermal effect on the proposed model is implemented by applying Arrhenius equations to make the model parameters variable with respect to the working temperature.

The parameters of this new model are identified through using a genetic algorithm. The model performance is validated by 24 discharge cycles, the sample battery of which is placed in a chamber, at three constant temperatures of 10 °C, 20 °C and 30 °C, respectively. Under the constant current conditions, the presented model has an average value RMSE of about 42 mV of battery terminal voltage. In addition, under three dynamic conditions, WLTC, NEDC and DST, the average RMSE value is about 15 mV of battery terminal voltage.

Future work will focus on mechanistic modeling of the rapid increase in transient polarization voltage at low battery SOC and efficiently extracting physical and chemical parameters of actual batteries to verify the reliability of the identified parameters.

Acknowledgement

The authors appreciate the financial support from the National Key Research and Development Program of China (Grant No. 2021YFF0601101).

References

[1] Subramanian V R, Boovaragavan V and Diwakar V D 2007 *Electrochemical and Solid-State Letters* **10** A225
[2] Mehta R and Gupta A 2021 *Electrochimica Acta* **389** 138623
[3] Li J, Lotf N, Landers R G and Park J 2017 *Journal of the Electrochemical Society* **164** A874
[4] Marcicki J, Canova M, Conlisk A T and Rizzoni G 2013 *Journal of Power Sources* **237** 310
[5] Luo W, Lyu C, Wang L and Zhang L 2013 *Journal of Power Sources* **241** 295
[6] Li C, Cui N, Wang C and Zhang C 2021 *Journal of Power Sources* **497** 229900
[7] Atlung S, West K and Jacobsen T 1979 *Journal of the Electrochemical Society* **126** 1311
[8] Wang Y, Zhang X, Liu K, Wei Z, Hu X, Tang X and Chen Z 2023 *Etransportation* **18** 100295
[9] Khaleghi R S, Rayman S and White R E 2013 *Journal of Power Sources* **224** 180
[10] Subramanian V R, Diwakar V D and Tapriyal D 2005 *Journal of the Electrochemical Society* **152** A2002
[11] Yuan S, Jiang L, Yin C, Wu H and Zhang X 2017 *Journal of Power Sources* **352** 245
[12] Lai Q, Jangra S, Ahn H J, Kim G, Joe W T and Lin X 2020 *Journal of Power Sources* **472** 228338
[13] Forman J C, Bashash S, Stein J and Fathy H 2010 *Proceedings of the ASME Dynamic Systems and Control Conference* **2** 178
[14] Smith K A, Rahn C D and Wang C 2008 *Journal of Dynamic Systems Measurement and Control-Transactions of the ASME* **130** 011012
[15] Smith K A, Rahn C D and Wang C 2007 *Energy Coversion and Management* **48** 2565
[16] Basdevant J L 1972 *Fortschritte Der Physik* **20** 283
[17] Ma S, Jiang M, Tao P, Song C, Wu J, Wang J, Deng T and Shang W 2018 *Progess in Natural Science-Materials International* **28** 653
[18] Liu H, Wei Z, He W and Zhao J 2017 *Energy Conversion and Management* **150** 304
[19] Chen Y, Kang Y, Zhao Y, Wang L, Liu J, Li Y, Liang Z, He X, Li X, Tavajohi N and Li B 2021 *Journal of Energy Chemistry* **59** 83
[20] Chen Y and Evans J W 1994 *Electrochimica Acta* **39** 517
[21] Wang Q, Shen J, Ma Z and He Y 2021 *Chemical Engineering Journal* **424** 130308
[22] Bahiraei F, Ghalkhani M, Fartaj A and Nazri G A 2017 *Applied Thermal Engineering* **125** 904
[23] Xu M, Zhang Z, Wang X, Jia L and Yang L 2015 *Energy* **80** 303
[24] Wang C Y and Srinivasan V 2002 *Journal of Power Sources* **110** 364
[25] Zhao R, Gu J and Liu J 2018 *International Journal of Energy Research* **42** 2728
[26] Liu F, Lan F and Chen J 2016 *Journal of Mechanical Engineering* **52** 141
[27] Wang Q, He Y, Shen J, Ma Z and Zhong G 2017 *Energy* **138** 118
[28] Panchal S, Dincer I, Agelin-Chaab M, Fraser R and Fowler M 2016 *Applied Thermal Engineering* **96** 190
[29] Dai H, Zhu L, Zhu J, Wei X and Sun Z 2015 *Journal of Power Sources* **293** 351
[30] Cheng X, Tang Y and Wang Z 2021 *Journal of the RMAL Science* **30** 477
[31] Xiong R and Li X 2020 *Journal of Mechanical Engineering* **56** 146
[32] Kuang K, Sun Y, Ren D, Han X, Zheng Y and Geng Z 2021 *Journal of Mechanical Engineering* **57** 10
[33] Allafi W, Zhang C, Uddin K, Worwood D, Truong Quang D, Ormeno P A, Li K and Marco J 2018 *Applied Thermal Engineering* **143** 472
[34] Ma Y, Mou H and Zhao H 2020 *Energy* **201** 117678
[35] Feng X, He X, Ouyang M, Lu L, Wu P, Kulp C and Prasser S 2015 *Applied Energy* **154** 74
[36] Ngoc T T, Farrell T, Vilathgamuwa M, Choi S S and Li Y 2019 *Journal of the Electrochemical Society* **166** A3059
[37] Prada E, Di Domenico D, Creff Y, Bernard J, Sauvant-Moynot V and Huet F 2012 *Journal of the Electrochemical Society* **159** A1508
[38] Jaguemont J, Boulon L and Dube Y 2016 *Applied Energy* **164** 99
[39] Bernardi D, Pawlikowski E and Newman J 1985 *Journal of the Electrochemical Society* **132** 5
[40] Doyle M, Fuller T F and Newman J 2018 *Journal of the Electrochemical Society* **165** X13
[41] Santhanagopalan S, Guo Q, Ramadass P and White R E 2006 *Journal of Power Sources* **156** 620
[42] Santhanagopalan S and White R E 2006 *Journal of Power Sources* **161** 1346
[43] Moura S J, Argomedo F B, Klein R, Mirtabatabaei A and Krstic M 2017 *IEEE Transcations on Control Systems Technology* **25** 453
[44] Xie Y and Cheng X 2021 *Electrochimica Acta* **399** 139391
[45] Xie Y and Cheng X 2022 *Journal of the Electrochemical Society* **169** 063516
[46] Hekmat S and Molaeimanesh G R 2020 *Applied Thermal Engineering* **166** 114759
[47] Ping P, Zhang Y, Kong D and Du J 2021 *Journal of Energy Storage* **36** 102448
[48] Jouhara H, Serey N, Khordehgah N, Bennett R, Almahmoud S and Lester S P 2020 *International Journal of Thermofluids* **1–2** 100004
[49] Baba N, Yoshida H, Nagaoka M, Okuda C and Kawauchi S 2014 *Journal of Power Sources* **252** 214
[50] Tanim T R, Rahn C D and Wang C 2015 *Energy* **80** 731
[51] Cai L and White R E 2009 *Journal of the Electrochemical Society* **156** A154
[52] Rodriguez A, Plett G L and Trimboli M S 2019 *Etransportation* **1** 100009
[53] Xu S, Wang Y, Shao J, Li J and Yu Q 2022 *Applied Thermal Engineering* **217** 119282